CHEMICAL DATA ASSIMILATION WITH TRACE-P FLIGHT MEASUREMENTS

T. Chai,[1] G. R. Carmichael,[1] A. Sandu,[2] Y. Tang,[1] and D. N. Daescu[3]

Tianfeng Chai, Center for Global and Regional Environmental Research, University of Iowa, 429 IATL, Iowa City, IA 52246, USA. (tchai@cgrer.uiowa.edu)

[1]Center for Global and Regional Environmental Research, University of Iowa, Iowa City, Iowa, USA.

[2]Department of Computer Science, Virginia Polytechnic Institute and State University, Blacksburg, Virginia, USA.

[3]Department of Mathematics and Statistics, Portland State University, Portland, Oregon, USA.

Abstract. In this paper, the four-dimensional variational (4D-Var) technique is applied to assimilate aircraft measurements of different chemical species during TRansport And Chemical Evolution over the Pacific (TRACE-P) field experiment into a chemical transport model, STEM-2K1. It is found that assimilating ozone observations from one of two independent flights improves model prediction of the other flight ozone measurements, which act as validation data. The adjusted initial fields after assimilating only NO_y observations lead to predictions of NO, NO_2, PAN that have better agreement with the reserved measurements. The key species whose initial mixing ratios would significantly affect the agreement between model and measurements can be identified using adjoint sensitivity analysis. We also find that enforcing concentration upper bounds in the optimization through L-BFGS-B algorithm is able to effectively speed up the data assimilation. One experiment simultaneously assimilating the observations of O_3, NO, NO_2, HNO_3, PAN, $PAN2$, and RNO_3 demonstrates that the model is able to match those measurements well by changing the initial fields. In addition, the model predictions of NO_y improve significantly after the assimilation. One test assimilating CO measurements suggests that the CO generation through the chemical reactions may be as important as the emissions. These results demonstrate how chemical data assimilation can be used to produce reanalysis fields that optimally use the information contained in both the measurements and the models.

1. Introduction

Chemical Transport Models (CTMs) have developed into a major tool in air quality and atmospheric chemistry analysis. Regional CTMs play an indispensable role in assessing, predicting, and interpreting the air quality-related hazardous events. On the other hand, large amounts of atmospheric chemistry observation data have been obtained through many field campaigns and a wide range of monitoring networks provide measurements on a regular basis. While CTMs and observations complement each other, the optimal analysis by integrating both components requires advanced data assimilation techniques.

Two methods have been extensively studied in meteorology and oceanography fields, the Kalman filter and the four-dimensional variational assimilation (4D-Var). It has become a common practice to build-in the assimilation of routinely available meteorological measurements into operational forecasting systems. The operational 4D-Var configuration has been implemented at the European Center for Medium-Range Weather Forecasts (ECMWF) [*Rabier et al.*, 2000; *Mahfouf and Rabier*, 2000; *Klinker et al.*, 2000]. The National Centers for Environmental Prediction (NCEP) has built an operational regional analysis-forecast system, the Rapid Update Cycle (RUC), using the 4D-Var with a hourly assimilation cycle [*Benjamin et al.*, 2004]. An operational implementation of Ensemble Kalman filter (EnKF) has been under development at the Canadian Meteorological Center (CMC) [*Houtekamer et al.*, 2005].

Advanced data assimilation in atmospheric chemistry was first carried out by *Fisher and Lary* [1995]. They applied 4D-Var to O_3 and NO_2 observations from the Upper Atmosphere Research Satellite (UARS), assimilating them into a simple chemistry model,

which included 6 species and 19 reactions. A Lagrangian scheme was adopted for the transport occurring in the stratosphere. They showed that data assimilation is capable of getting synoptic analysis from asynoptic observations. *Elbern et al.* [1997] developed the adjoint model of EURopean Air pollution Dispersion model (EURAD), a regional Eulerian model that focuses on tropospheric chemistry, and have used it in various studies [*Elbern and Schmidt*, 1999; *Elbern et al.*, 2000; *Elbern and Schmidt*, 2001; *Hoelzemann et al.*, 2001]. *Errera and Fonteyn* [2001] presented a stratospheric chemical assimilation system with a 3-dimensional (3-D) CTM using 4D-Var, and applied it to the Cryogenic Infrared Spectrometers and Telescopes for the Atmosphere (CRISTA) measurements. Other Eulerian 3-D CTMs that have developed adjoint models include STEM-2K1 (Sulfur Transport Eulerian Model, version 2K1) [*Daescu and Carmichael*, 2003; *Carmichael et al.*, 2003a; *Sandu et al.*, 2005], and the CHIMERE model [*Menut et al.*, 2000; *Schmidt and Martin*, 2003; *Menut*, 2003].

In addition to the variational data assimilation work, there are a number of atmospheric chemistry data assimilation applications using the Kalman filter approach. Without the requirement of developing adjoint models, more CTMs have been used in Kalman filter data assimilation experiments. These include the regional models LOTOS (Long Term Ozone Simulation) [*Segers et al.*, 2000; *van Loon et al.*, 2000] and EUROS (EURopean Operational Smog) [*Zhang et al.*, 1999; *Hanea et al.*, 2004]. The global CTM MOZART (Model for OZone And Related Tracers) has been used to assimilate satellite CO observations [*Clerbaux et al.*, 2001; *Lamarque and Gille*, 2003; *Lamarque et al.*, 2004], as well as to constrain tropospheric ozone columns (TOC) [*Lamarque et al.*, 2002].

The variational data assimilation approach can be applied to initial state (i.e., initial conditions) and parameter estimation (including emissions), and used in forecasting and inverse modeling of emissions. Another important application of data assimilation is in the reanalysis of field data. It is our premise that the value derived from large field experiments can be enhanced by a closer integration of modeled and measured quantities, with the two merged together to provide a consistent and best estimate of the chemical state of the atmosphere. In formal data assimilation the intent is to optimally use the observations (reality within errors) along with the model (imperfect representation of the processes and their connections) to produce a better estimate (in some optimal sense) of the chemical state of the atmosphere. There are many possible approaches to this and 4D-Var is one of them.

In this paper we demonstrate how 4D-Var can be used in the reanalysis of aircraft data. We use the 4D-Var technique to assimilate aircraft measurements from the Transport And Chemical Evolution over the Pacific (TRACE-P) mission into the STEM-2K1 model. We present the basic 4D-Var assimilation framework, demonstrate and explore various issues related to the assimilation of ozone, NO_y and CO observations. These results are discussed in terms of how reanalysis fields can be produced using 4D-Var. Results for mission-wide reanalysis will be presented in a future paper.

2. 4D-Var Data Assimilation Method

2.1. Chemical transport model

STEM-2K1 is a regional CTM, which in this study uses the SAPRC-99 chemical mechanism [*Carter*, 2000]. In total 235 gas phase reactions and 93 chemical constituents are included in this mechanism. In the model, the evolution of the chemical constituent

concentration vector c in time (t) is described as

$$\frac{\partial c}{\partial t} = -u \cdot \nabla c + \frac{1}{\rho}\nabla \cdot (\rho K \cdot \nabla c) + \frac{1}{\rho} f + E \tag{1}$$

Here we denote by u the wind field vector, ρ the air density, K the turbulent diffusivity tensor, f the chemical transformation rate, and E the rate of elevated emissions. The boundary conditions are

$$c(t,x) = c^{\mathrm{IN}}(t,x) \quad \text{for} \quad x \in \Gamma^{\mathrm{IN}}, \tag{2a}$$

$$k_{nn}\frac{\partial c}{\partial n} = 0 \quad \text{for} \quad x \in \Gamma^{\mathrm{OUT}}, \tag{2b}$$

$$k_{nn}\frac{\partial c}{\partial n} = V^{\mathrm{dep}} c - Q \quad \text{for} \quad x \in \Gamma^{\mathrm{GR}}. \tag{2c}$$

where n is the unit outward normal vector on the domain surface, and $k_{nn} = n \cdot K \cdot n$. V^{dep} is the deposition velocity. Q is the rate of surface emissions. Γ^{GR} stands for the ground surface boundary. Lateral boundaries are partitioned into inflow Γ^{IN} and outflow Γ^{OUT} regions. On the domain top, concentrations are fixed.

In STEM-2K1, the evolution is solved using an operator splitting approach, in which the transport along each direction and the chemistry steps are taken successively. A Rosenbrock method is used as the chemistry solver. The Kinetic PreProcessor (KPP) tool [*Sandu et al.*, 2003; *Daescu et al.*, 2003] was used to generate both the forward and the adjoint chemistry code. A detailed description on STEM-2K1 model can be found in *Carmichael et al.* [2003b].

2.2. Adjoint of STEM-2K1

The adjoint of STEM-2K1 is described in detail in *Carmichael et al.* [2003a]. *Daescu et al.* [2000] shows the derivation of the adjoint of the Rosenbrock scheme. Here we only

give a brief description of the adjoint model. The adjoint of the tangent linear model of STEM-2K1 defines the evolution of the adjoint variable vector λ, which reads as

$$\frac{\partial \lambda}{\partial t} + \nabla \cdot (u\lambda) = -\nabla \cdot \left(\rho K \cdot \nabla \frac{\lambda}{\rho} \right) - (F \cdot \lambda) - \phi \tag{3}$$

In this equation ϕ is a forcing functional vector and will be defined in section 2.3. F is a tensor function, obtained by linearizing the incremental f as $\delta f \approx F \cdot \delta(\rho c)$. As f is a nonlinear function of (ρc), F also varies with (ρc), i.e. $F = F(\rho c)$. The corresponding boundary conditions are

$$\lambda(t, x) = 0 \quad \text{for} \quad x \in \Gamma^{\text{IN}}, \tag{4a}$$

$$\lambda u_n + \rho k_{nn} \frac{\partial(\lambda/\rho)}{\partial n} = 0 \quad \text{for} \quad x \in \Gamma^{\text{OUT}}, \tag{4b}$$

$$\rho k_{nn} \frac{\partial(\lambda/\rho)}{\partial n} = V^{\text{dep}} \lambda \quad \text{for} \quad x \in \Gamma^{\text{GR}}. \tag{4c}$$

To obtain the ground boundary condition we use the fact that $u_n = u \cdot n = 0$ at ground level. $\lambda(t, x) = 0$ holds on the top boundary. Note that the adjoint initial condition is posed at the final time T.

The adjoint system (3)–(4) depends on the state of the forward model (i.e. on the concentration fields $c(x, t)$) through the nonlinear chemical term $F = F(\rho c)$ and the forcing term ϕ resulted from nonlinear cost functionals. This means that the forward model must be first solved, the state $c(x, t)$ saved for all t, then the adjoint model is integrated backward in time from T down to t^0.

2.3. Cost functional and minimization

In 4D-Var the optimal solution minimizes the cost functional, which is generally defined as

$$J = \frac{1}{2} \left[c_0 - c_b \right]^T B^{-1} \left[c_0 - c_b \right] + \frac{1}{2} \left[y - h(c) \right]^T O^{-1} \left[y - h(c) \right] \tag{5}$$

where B and O are error covariance matrices for background and observations in discrete spaces, respectively. h is a projection operator, calculating the observation vector $y = y(x,t)$ from the model space $c = c(x,t)$. In the current study the initial concentrations $c_0 = c(t=0)$ are chosen as the only control parameters to adjust, but in principal any model parameters including emissions can be adjusted. Hereafter, the subscript "0" is used to denote variables at instant $t = 0$. Assuming that the operator h is linear, $h(c)$ can be written as $h(c) = H \cdot c$. In our application, H reflects trilinear interpolation in space and linear interpolation in time when constructing model counterparts of the observations. For NO_y measurements by the NASA P3-B aircraft, the model counterpart is calculated from the modeled species as

$$\begin{aligned}[NO_y] \;=\; & [NO] + [NO_2] + [NO_3] + 2 \times [N_2O_5] + [HONO] + [HNO_3] \\ & + [HNO_4] + [RNO_3] + [PAN] + [PAN2] + [PBZN] + [MA\_PAN] \end{aligned} \tag{6}$$

It is also represented in the H transformation matrix ("[ ]" represents the concentration. PAN: peroxy acetyl nitrate; RNO_3: lumped organic nitrates; $PAN2$: PPN (peroxypropionyl nitrate) and other higher alkyl PAN analogues; PBZN: PAN analogues formed from aromatic aldehydes; MA_PAN: PAN analogue formed from methacrolein).

The forcing term ϕ in equation (3) appears as

$$\phi = H^T \cdot O^{-1} \cdot [y - H \cdot c] \tag{7}$$

The backward integration of equation (3) gives adjoint variables at any time, which are the sensitivities of the cost functional with respect to state variables (concentrations), i.e.

$$\delta J = \lambda^T \cdot \delta c \tag{8}$$

Note that the background part of the cost functional in equation (5) adds one more term to the gradient of the cost functional with respect to initial concentrations. Using equation (5), we have

$$\delta J = \left[\lambda_0^T + (c_0 - c_b)^T \cdot B^{-1}\right] \cdot \delta c_0 \tag{9}$$

where $\lambda_0^T + (c_0 - c_b)^T \cdot B^{-1}$ is the gradient information needed for the minimization. The optimal initial condition c_0 can be found efficiently by applying many different minimization routines. Quasi-Newton limited memory L-BFGS [*Byrd et al.*, 1995] is used by most 4D-Var applications. In this article, an updated version, L-BFGS-B [*Zhu et al.*, 1997] is used. We found that adding bound constraints improve the computation efficiency. This is discussed further in section 3.3.3.

It is worth to note that we choose to seek the optimal solution of $ln(c_0/c_r)$ rather than c_0 in the minimization. The reference concentration c_r, with unit values, is introduced to make $ln(c_0/c_r)$ unitless. The logarithm change of control variables acts as a crude preconditioning in the optimization, and it was implemented by *Elbern et al.* [1997]. For convenience, the background term is also changed to

$$\frac{1}{2}\left[\ln\frac{c_0}{c_r} - \ln\frac{c_b}{c_r}\right]^T U^{-1}\left[\ln\frac{c_0}{c_r} - \ln\frac{c_b}{c_r}\right] \tag{10}$$

which can be simplified as

$$\frac{1}{2}\left[\ln c_0 - \ln c_b\right]^T U^{-1}\left[\ln c_0 - \ln c_b\right] \tag{11}$$

Here U is then taken as the error covariance matrix of $ln(c_0/c_r)$. A similar relation as equation (7) is found as

$$\delta J = \left[(c_0\lambda_0)^T + (\ln c_0 - \ln c_b)^T \cdot U^{-1}\right] \cdot \delta \ln c_0, \tag{12}$$

where $(c_0\lambda_0)$ represents a component-by-component multiplication and the result is still a vector. In the current study the predictions using the same CTM from the previous analyses [*Carmichael et al.*, 2003b] were chosen as the background fields. Lacking knowledge of the background error statistics to know B or U, we assume U to be a diagonal matrix and then assign 1000 to all diagonal components. It is equivalent to setting the uncertainty of $ln(c_0/c_r)$ as 31.6, which implies that the background field is considerably more uncertain than the measurements so that the data assimilation is mainly driven by the observations. In our data assimilation analyses, the optimization proceeds until the cost functional is reduced to 0.001 of its initial value, or the number of forward-backward model integrations exceeds 20.

3. Data Assimilation Analysis

3.1. Observations and model setup

As part of the NASA Global Tropospheric Experiment (GTE), the TRACE-P aircraft mission was conducted in February-April 2001. To demonstrate the utilization of the 4D-Var technique to flight observations, we only use measurements from two flights, flight 7 of the DC-8 and flight 9 of the P3-B. The observations are 5-min averaged, and run through 1:12–10:45 GMT for the DC-8 and 2:20–10:00 GMT for the P3-B. The coverage of the two flight routes is given in Figure 1, while Figure 2 displays the flight heights and the distances between two aircrafts as three time series. The DC-8 has a higher ceiling, and greater range than the P3-B, but it has to climb to above 8 km altitude to cool off after operating below 3 km for more than about an hour.

The aircraft measurement errors are assumed to be uncorrelated, thus the observation error covariance O is a diagonal matrix. The variances are obtained by approximating the

measurement uncertainty for O_3, NO_y, NO, NO_2, and CO to be 8%, 18%, 20%, 20%, and 1%, respectively. Measurement uncertainty for other species are all assigned 100%.

STEM-2K1 was run with a $90 \times 60 \times 18$ grid, and a horizontal resolution of 80km $\times$ 80km. Sigma-z coordinate system is used in the vertical direction, following the RAMS dynamic model [*Pielke et al.*, 1992], which also provides the meteorological fields to STEM-2K1. Figures 3 and 4 display the wind fields at 0 GMT and 9 GMT, at altitudes of 3.5 km and 1.0 km respectively. The flow situation on this day was dominated by a low pressure system located in the upper right corner of the domain. Strong continental outflows associated with these flows transported pollutants from Southeast Asia (including pollutants associated with biomass burning in Thailand and Mynammar) into the western Pacific. This outflow of pollutants from southeast Asia was maximum at altitudes between 2–4 km. Flows below 2 km were typical of the winter monsoon, and these southerly flows transported pollutants from coastal China to the lower latitudes. The flights on this day were designed to sample the continental outflow in this frontal system. Further details of the transport of pollutants in this frontal system can be found in *Carmichael et al.* [2003b]. The emission inventories implemented here are presented in *Streets et al.* [2003] and *Woo et al.* [2003].

All data assimilation analysis runs have the time window of 0:00–12:00 GMT, which covers the entire period of these two flights. Both the forward and adjoint models are parallel and implemented using the Parallelization library for Air Quality Models on Structured Grids (PAQMSG) [*Miehe et al.*, 2002].

3.2. O_3 assimilation

In this section, we present the data assimilation results of two tests, in which O_3 measurements by the DC-8 and the P3-B are assimilated separately. The ozone measurements were obtained by M. Avery from NASA Langley.

3.2.1. Data assimilation

In these two tests, initial O_3 concentrations are chosen to be the only control variables to be adjusted. Figure 5 shows the time series of model predictions of O_3 concentrations from the two tests, as well as the original observations. Without data assimilation the STEM-2K1 predictions reproduce the overall trend of the DC-8 O_3 measurements, but consistently miss the low values at 7:00 GMT, 8:00 GMT, 9:00 GMT, and 10:00 GMT. For the P3-B flight measurements, the model results appear to be too smooth in time compared to the measurements.

After data assimilation, the CTM can better match the flight measurements. While the case using the DC-8 measurements yields better agreement, there remains discrepancies between the model and the P3-B observations after assimilation. As the P3-B flew slower and covered a smaller region, its measurements represent some spatial variations that are difficult for the CTM to reproduce at the current resolution. The time series of P3-B measurements shows O_3 concentrations over 100 ppbv at about 4:00 GMT and 8:30 GMT. The locations of these two instances are close to each other, at $(121E, 21N)$, and the flight altitudes are $\sim$ 2.7 km for both instances. This region of high O_3 appears to be associated with the biomass burning-influenced outflow from Southeast Asia (see Figure 5). The placement and timing of this elevated plume-like structure in the warm sector of this frontal system is difficult to accurately predict. So the model is blind

to the structure unless observations are actually injected into the model through data assimilation. The DC-8 only flew past that region once, at 4:00 GMT, but at a much higher altitude (> 6 km). Thus the DC-8 failed to pick up the high concentrations.

3.2.2. Validation

After assimilating observations from the two flights separately, we applied the updated initial condition to predict measurements from the other flight which were not used in the previous data assimilation tests. Results are also shown in Figure 5. The in-situ aircraft measurements only sample along the flight route and thus provides limited information with respect to the four-dimensional space (i.e. three-dimensions in space plus one dimension in time). The limited information brought into the model by data assimilation is expected to have minimal effect on the model predictions at grid points that are not close to the assimilated observations.

Figure 5 demonstrates only slight improvement of the model prediction on the held observations of one flight O_3 measurements after assimilating the other flight. For both tests, the agreement between measurement and model results becomes better at the beginning and the end of the flights. This is due to the fact that both flights took off from and landed at the same base, shown by Figure 1. Note that the two aircrafts were not close to each other at any instance during the flight, as there was about one hour difference in both take-off and landing time between the two aircrafts. Figure 2 shows that the closest distance between the DC-8 and the P3-B was about 500 km, i.e. about 6 grid-cells, when the P3-B was about to land. This result reveals that the effect of the assimilated measurements is felt most strongly in their neighboring grid points.

While the measurements from the two flights are independent, the two tests also serve the validation purpose. Although assimilating the flight measurements does not change the model predictions of the other flight significantly, the modifications that the assimilation incurred were almost exclusively found to improve the agreement between the model and the validation observations. For example, model predictions of O_3 along P3-B flight route clearly became better during the period of 3:40–4:40 GMT after assimilating the DC-8 O_3 measurements. Between 3:40 GMT and 4:40 GMT, the STEM-2K1 model predicted higher O_3 concentrations than the DC-8 measurements before data assimilation. After assimilating the lower DC-8 O_3 measurements to bring down the corresponding model results, the predicted values for the P3-B actually increased during this period, resulting in a better match between the model and measurements.

A further look at the flight routes suggests that the better model results at 3:40–4:40 GMT along the P3-B path is mainly due to the assimilation of DC-8 measurements at an earlier time. During the period of 3:40–4:40 GMT, the P3-B flew from (120.52E, 20.74N) to (124.02E, 23.65N), with the altitude ranging from 2 km to 3 km. The DC-8 flew in the neighborhood of this region at 2:25–2:45 GMT. During the time, the DC-8 flew from (121.91E, 20.83N) to (123.39E, 22.00N), with an altitude of about 3km. This partially reflects the merit of having better earlier information on the improvement of the CTM predictions. In practice, it is almost impossible for CTMs to have accurate 3D initial conditions. Although measurements are often available, they are scarcely distributed in space and time. Variational data assimilation provides a mathematically sound technique to utilize these observations.

To shed more light on the improvement of the model predictions on the P3-B measurements after the assimilation of the DC-8 O_3 measurements, we built a new cost functional only using the P3-B O_3 measurements between 3:40 GMT and 4:40 GMT. An influence function $\mathcal{C}(x)$ is calculated to show the regions that significantly affect model predictions corresponding to the selected observations. $\mathcal{C}(x)$ is obtained by averaging the magnitudes of adjoint sensitivities over time, i.e.

$$\mathcal{C}(x) = \frac{1}{N} \sum_{n=0}^{N-1} |\lambda(x,t)|, \tag{13}$$

where N is the total number of time steps. This can be calculated for any species, showing their effects on the specific predictions corresponding to the selected observations. The spatial distribution of $\mathcal{C}(x)$ shows the "cones of influence" (see *Sandu et al.* [2005] for details). Figures 6 and 7 display the projections of the "cones of influence" by ozone. It is clearly seen that the knowledge of ozone concentration in two regions is most helpful to the predictions of the selected observations and they were both covered by the DC-8 flight. As expected, the region that affects the specific predictions is located around the target region, i.e. where the P3-B O_3 measurements were made. The other part is located to the north of the target, with an altitude around 1km where the wind was mainly due south. However, the DC-8 flew past the region around 4:00 GMT. It is speculated that if the DC-8 had flown the region at an earlier time, the observations would be more beneficial to the model predictions.

For the previous tests that assimilated O_3 measurements, only the initial O_3 concentrations were adjusted. As a complete chemistry mechanism is included in STEM-2K1, changes of other species at initial time would also affect O_3 predictions by the model. An almost identical result was found when we tried to assimilate O_3 measurements by

adjusting initial concentrations of 55 species. This is due to the fact that for these flights the air masses sampled by the aircrafts were well aged (typically several days old). This is not a general finding as assimilating measurements of other species often require adjusting initial concentrations of more than one species. In the following section, we present the results from assimilating the P3-B NO_y observations.

3.3. NO_y assimilation

3.3.1. Assimilation

NO_y was measured on-board the P3-B and provides another important example of data assimilation. NO_y is an integrated measurement that represents many individual species (the species that are included in the model that comprise NO_y are shown in Equation (6)). Assimilation of NO_y provides the possibility of improving the predictions of many individual species by the assimilation of a single observation. Below we present results from the assimilation of the NO_y observations. The NO_y measurements were obtained by Y. Kondo's group at the University of Tokyo.

The model predictions of NO_y are obtained using equation (6). NO and NO_2 were chosen as the only species to adjust in our first experiment to assimilate NO_y measurements. Model predictions of NO_y before and after the data assimilation are shown in Figure (8), as well as the original observations. The significant discrepancy between model predictions and measured NO_y between 3:30 GMT and 4:00 GMT is corrected after assimilation. The other noticeable improvement of the NO_y predictions happen between 6:00 GMT and 7:00 GMT, as well as at the take-off and landing times. There are still differences between the model and observations, especially around 8:30 GMT, and during 4:30–6:00 GMT. Two other experiments were made, each by adjusting one additional species. In the first,

the initial PAN was also adjusted, as its concentration is larger than other components in equation (6) based on the observations. In the second, O_3 was chosen as the additional control variable since it is closely involved in the NO and NO_2 reactions. The results of these two cases are also shown in Figure 8. It is found that adding O_3 does not help the data assimilation much, as this addition almost generates the identical results as the case that has NO and NO_2 as control variables. This is also consistent with the previous result, where assimilation of O_3 data had little effect on NO and NO_2. On the other hand, the addition of PAN to the control variables helps the model to produce predictions that better match observations around 5:15 GMT and during 6:00–7:00 GMT than the two previous cases.

Figure 8 also shows two other cases conducted to assimilate the NO_y measurements. The case that included the initial NO, NO_2, HNO_3, PAN, and $PAN2$ as control variables is able to re-generate the NO_y peak value at 8:30 GMT. In another test, we included the initial concentrations of all prognostic species as control variables. There are 66 prognostic species in our STEM-2K1 model, but 16 of them are not involved in NO_y prediction. So we chose 50 species as control variables. The results of this case show the best agreement between the predictions and assimilated observations.

3.3.2. Adjoint sensitivity analysis

In theory, we can always choose the concentrations of all species at the initial time as control variables if an adequate preconditioning is performed before or during the minimization. However, the large number of control variables will make the full background error covariance estimate B in equation (5) impractical to implement even when statistics are available. Eliminating the species that have minimal effect on the model predictions of

certain observations from the control variables improves the conditioning in the minimization, and thus is beneficial in the 4D-Var data assimilation. In the case that the initial concentrations of 50 species are chosen to be adjusted, the number of control variables is $90 \times 60 \times 18 \times 50 = 4,860,000$. The implementation is made possible by assuming B or U in equation (10) to be diagonal.

The key species that affect the model predictions of certain measurements can be effectively found out using the 4D-Var data assimilation system. To seek those key species, we look at the gradients of the cost functional, i.e. $\partial J/\partial \ln c_0$, which is equal to $\lambda \cdot c_0$ and can be easily obtained through the adjoint model in the current 4D-Var data assimilation system. Here the cost functional is defined as equation (5), measuring the difference between the measurements and model output in a least square form. For instance, the 5 species chosen in the previous case to assimilate NO_y measurements are based upon such sensitivity analysis. Figure 9 shows the horizontally averaged magnitudes of the gradients for each prognostic species at 18 model vertical levels (The vertical grid distance is increasing with the height. The altitude of level 5 is 1.0 km and level 10 is at 3.5 km). The averaged magnitudes are calculated by averaging the absolute values of the gradients. The magnitudes indicate which species and at what levels would most drastically affect the model predictions of the measurements that are used to construct the cost functional. Based on Figure 9, NO, NO_2, HNO_3, PAN, and $PAN2$ are the key species that affect the NO_y predictions for this case.

The mean value of $\partial J/\partial \ln c_0$ on each level is displayed in Figure 10. This metric identifies whether the overall increases or decreases in the initial concentrations of individual species are needed to reduce the cost functional, i.e. to improve the model predictions.

Figure 10 shows that $\partial J/\partial \ln c_0$ is mostly positive for NO, NO_2, HNO_3, PAN, and $PAN2$ at the lower levels. This implies that we need to reduce the initial concentrations of these species to better match the measurements. Around level 10, which is 3.5 km, the aforementioned components need to increase their concentrations, to best match to the observations. It is consistent with the model predictions of NO_y before assimilation shown in Figure 8. The model tends to underestimate NO_y at higher altitudes and overestimate slightly at lower altitudes. The underestimation of NO_y at higher altitudes is likely due to slight misplacement of the biomass burning air masses from Southeast Asia.

Figure 11 shows the averaged magnitude and mean of the sensitivity, with the cost functional representing the differences between P3-B O_3 measurements and their model counterparts. We see that the model predictions of O_3 along the P3-B flight track are much more sensitive to the initial O_3 field than any other species. It explains why we were able to assimilate the O_3 measurements well by only adjusting initial O_3 concentrations. In general, photochemically active species such as NO_2 are tightly connected to many species. For instance, similar analysis applied to NO_2 measurements shows that initial O_3, CO, and NO affect NO_2 as much as its own initial condition. Unlike NO_y, the model prediction of O_3 is very sensitive to the initial O_3 mixing ratios over the domain top due to the stratospheric O_3 source. A positive mean gradient shown in Figure 11 implies that a reduction of the O_3 mixing ratios at the top would bring the model prediction of O_3 closer to the P3-B O_3 measurements. With a negative gradient in the middle vertical layers, where the P3-B flew most of the time, the initial O_3 appears to be underestimated (Figure 5 shows the model predictions are generally lower than the measurements). At lower altitudes when the P3-B flew around 7:00 GMT and 9:00 GMT, the measurements

are lower than predicted. Figure 11 displays the positive mean gradients at lower levels, suggesting the initial O_3 should be reduced in order to produce a better match between the model and measurements.

3.3.3. Minimization algorithm

In 4D-Var, the L-BFGS algorithm is often chosen to update the control variables en route to the minimization of the cost functional. Without the need to save a full Hessian matrix, it proves to be very effective in optimization problems that have a large number of control variables. However, the minimization algorithm is not immune to the generation of physically or chemically unrealistic points in its line-search procedure. For instance, if the initial mixing ratio c_0 is chosen as the control variable, the line-search cannot guarantee to generate all positive components at the next point unless such a requirement is explicitly stated. Negative mixing ratios can be avoided by choosing $ln(c_0/c_r)$ as control variable, which ensures positive c_0 by the relation

$$c_0 = c_r e^{\ln \frac{c_0}{c_r}}. \tag{14}$$

Solely a mathematical procedure, the line-search can still end up with some unrealistic values in its pursuit of the optimal solution, such as 1000 ppbv O_3 mixing ratio in the troposphere. Such points are destined to be thrown away since they differ too much from the background, and the forward model integration using them would produce results far away from the real measurements. Thus a large cost functional would be generated and the line-search has to restart from the previous spot. Normally the iteration number reported in the optimization does not count such miscues although it is costly to waste time-consuming CTM forward integrations and backward adjoint runs. In the current study, as described before, we set the maximum forward-backward integrations to be 20.

Additional information about the expected range of the chemical species mixing ratios can be effectively included into the minimization using the L-BFGS-B algorithm (The last "B" of L-BFGS-B stands for "bounds". The algorithm is able to solve large-scale bound-constrained or unconstrained optimization). The upper bounds for each species at every level can be specified. For instance, the NO_2 mixing ratio upper limits at the bottom and top levels (z=0.075 km, 15.179 km) were set to be 30 ppbv and 0.5 ppbv respectively, while the O_3 upper bounds were set to 200 ppbv throughout the domain (These values were determined based on the TRACE-P observations). Figure 12 shows the NO_y assimilation results using the 5 aforementioned species as control variables, when the upper limit of these mixing ratios were enforced through the upper bounds in the L-BFGS-B algorithm. The previous test using the same controls, but without the upper bounds, is also shown for comparison. The benefit of adding the upper bounds through L-BFGS-B algorithm is clearly shown in the figure. In fact, the new result is very comparable to the one using 50 control variables shown in Figure 8. Applying the upper bound constraint for the case using 50 control variables shows slight improvement as well. For these L-BFGS-B implementations, about 0.3% of the constraints are active. It should be noted that to minimize with L-BFGS and then apply the upper-limit constraint by replacing those large values is not equivalent to enforcing the upper bound inside the L-BFGS-B algorithm.

3.3.4. Model response on NO_y assimilation

In section 3.2 we showed that improvement of the model predictions by assimilating O_3 measurements extends hundreds of kilometers away from the measurements. In fact, assimilating measurements of one kind can have positive effects on many other closely related species. Figure 17 shows the model predictions of NO, NO_2, HNO_3, PAN,

$PAN2$, and RNO_3, before and after assimilating the P3-B NO_y measurements. The measurements of these species by the P3-B are also plotted to evaluate the assimilation effect, but they were kept from the data assimilation test. The data assimilation presented here uses 50 control species and applies the L-BFGS-B algorithm.

The model predictions of NO, NO_2, and PAN significantly improve around 4:00 GMT after assimilating the NO_y observations. This is consistent with the fact that the large discrepancy between model predicted and measured NO_y between 3:30 GMT and 4:00 GMT is reduced in the data assimilation, as displayed in Figure 8 and Figure 12. The model results of NO_y also change greatly at around 8:30 GMT after assimilation, as shown in Figure 12. This translates to the close agreement between model predictions of NO after assimilation and the actual NO measurements by the P3-B which are not assimilated. Another significant improvement made by assimilating NO_y is on the PAN prediction during 5:00–7:00 GMT. The model results do not change much at the other times. For species that do not contribute to NO_y directly under these conditions), such as O_3, the model has little response. There is almost no change of RNO_3 predictions after assimilating NO_y measurements.

After assimilating the P3-B NO_y measurements, the adjustments on the initial conditions on the chosen 50 control species are quite different. The most significant relative changes over the original initial values are on the initial O_3, NO_2, HNO_3, and PAN. For each species,

$$\mathcal{R}(x) = \frac{c_0(x) - c_b(x)}{\overline{c_b(x)}} \tag{15}$$

is calculated, where $\overline{c_b(x)}$ is the average of the background mixing ratios. Figures 13–16 show $\mathcal{R}(x)$ on two slices. While the drastic changes are located around the flight region,

the adjustment of the initial conditions reaches much further. The changes are not simple increases or decreases, and show various patterns for different species. While the patterns share more similarity between NO_2, HNO_3, and PAN, that of O_3 is distinctive in that it reaches more eastward and further in height. Due in part to the long lifetime of ozone in the upper troposphere and the contributions of stratospheric/tropospheric exchange processes. As Figure 3 shows westerly winds at z=3.5 km in the P3-B flight region, the adjustments on the initial conditions of NO_2, HNO_3, and PAN shift to the west of the P3-B flight route, reflecting the transport effect.

We should note that many different combinations of the components can lead to the same NO_y value. Thus no unique solution is guaranteed only based on NO_y measurements. The presence of the background term in equation (5) is meant to guarantee the uniqueness of the optimal solution. In other words, among the many possible combinations that give results matching observations, we choose the solution that is "closest" to the background field. The constraint brought by the measurements is capable of detecting and correcting the apparent discrepancy between model and observations, such as that shown at 3:40–4:00 GMT in Figure 8. The assimilation of NO_y leads to better model predictions of NO and NO_2, which would be difficult to obtain otherwise. Given enough information on the statistics of the background error and the observation uncertainty, an optimal solution can be obtained based on the minimization of the cost functional shown in equation (5).

3.4. Other assimilation tests

3.4.1. Assimilation of multiple observation species

In the previous tests we focused on the effect of assimilating measurements of a single parameter in the CTM analysis. In this section, we present results from simultaneously assimilating O_3, NO, NO_2, HNO_3, PAN, and RNO_3 observations measured by the P3-B. The NO and NO_2 measurements were taken by Y. Kondo's group at the University of Tokyo, HNO_3 by F. Eisele, Georgia Institute of Technology, PAN by F. Flocke, NCAR, and RNO_3 by E. Atlas, NCAR. The initial concentrations of the same 50 prognostic species, as in the NO_y assimilation, were used as control variables. Upper bounds were enforced in the L-BFGS-B algorithm.

Figure 18 shows measurements and the predictions of the 6 assimilated species. As expected, the overall prediction improved when adding additional assimilated species. In the first half of the assimilation time window the improvements over model predictions are visible for all species except for RNO_3. In the second half, the improvement is not as strong, but still shows the positive effect of assimilation. Since the O_3 measurements are the most accurate, with an estimated uncertainty of 8%, it is the major component in the cost functional defined in equation (5). The minimization of the cost functional then drives the model predictions to match O_3 measurements as the primary task. The uncertainties for NO and NO_2 are 20%, much smaller than the uncertainties assumed for HNO_3, PAN, and RNO_3, which are 100%. This leads to slightly better agreement between model and observations for NO and NO_2 than for HNO_3, PAN, and RNO_3 after assimilation.

It is interesting to note that the forward model performs poorly during 3:40–4:00 GMT along the P3-B route, and clearly misses a pollution plume. The large discrepancy between the model and measurements can be efficiently reduced by assimilating just a little relevant

information. For instance, O_3 prediction during this time is improved by assimilating the independent O_3 measurements by the DC-8. NO and PAN are also much close to the measurements if only NO_y measurements are assimilated into the model. This proves the value of integrating the observations with the CTM through data assimilation.

Figure 19 shows the NO_y calculated by the model after assimilation of observed NO, NO_2, HNO_3, PAN, and RNO_3, to the observed values of NO_y. Since the NO_y measurements were not used in the assimilation and are independent of the observations that were assimilated, it also serves as a validation test. The results demonstrate that the assimilation of various observations on species comprising NO_y significantly improves the model predictions of NO_y. Unlike the early validation test using measurements from two different flights, here the held NO_y observations and the assimilated measurements from the same flight share the same spatial and temporal sampling patterns. Thus, the impact of the assimilation is no longer limited by the transport distances and the improvement of NO_y is throughout the whole flight.

An additional simulation was performed where we simultaneously assimilated measured NO_y and NO, NO_2, HNO_3, PAN, and RNO_3. This assimilation also produced slightly different results. A comparison of the effect of assimilation of NO_y only, assimilation of NO, NO_2, HNO_3, PAN, and RNO_3 together, and the assimilation of NO_y along with NO, NO_2, HNO_3, PAN, and RNO_3 is shown in Figure 20. As discussed above assimilation of NO_y by itself does not provide a unique solution to the adjustment of the various species contributing to NO_y. Adding additional species in theory adds determinism, but in the optimization of the competing pieces of information leads to a spectrum of results. For example, contributions of PAN to NO_y just before 4 GMT and at $\sim$ 5 GMT are

significantly different for the three cases. The fact that the results are not consistently improved with more information may reflect a systematic error in the forward model (e.g., in regards to a deficiency in the chemical mechanism), correlations between measurement errors (not accounted for in these results), and /or errors in other parameters not adjusted in these initial condition-only adjustments (e.g., emissions). Further studies are on-going into these aspects and will be the subject of future papers.

3.4.2. *CO* assimilation

CO is another important species for reanalysis. In the following test, the *CO* observations measured on the DC-8 by G. Sachse, NASA, Langley, were assimilated. If only initial *CO* is allowed to be adjusted in the data assimilation, the model predictions of *CO* show little improvement (results not shown). An adjoint sensitivity analysis reveals that the initial ozone, aldehydes and primary non-methane hydrocarbons are critical in determining *CO* predictions, as well as the initial *CO* (see Figure 21). Further more, the maximum sensitivities are found at altitudes between 2–4 km, in the region of the Southeast Asia outflow. Figure 22 shows the assimilation results by adjusting the same 50 species as the previous cases. Before the assimilation, the CTM under-predicted the *CO* mixing ratios most of the time. A good match between the CTM predictions and observations is achieved after the assimilation. These results also have implications for inverse modeling of *CO* emissions. Typically *CO* inversions are done in a pseudo tracer mode, where the generation of *CO* from the non-linear photochemical reactions involving non-methane hydrocarbons are not explicitly taken into account. The 4D-Var technique takes these reactions into account, and can recover (simultaneously) initial conditions

and/or emissions. The inversion of CO emissions using the TRACE-P data will be the subject of a future paper.

4. Summary

We presented variational data assimilation analyses using TRACE-P flight measurements and STEM-2K1 chemical transport model. By adjusting certain initial chemical fields, the CTM can generate results that closely match the observations. Using the adjusted initial field after assimilating O_3 measurements, the agreement between model predictions and measurements by the other independent flight improves. It is also found that the model predictions of NO, NO_2, and PAN better match the measurements when only NO_y observations are assimilated. The case that assimilates measurements of different species shows the effect of different observations used in the assimilation highly depends on the their measurement uncertainties.

In this study we also showed the benefit of adjoint sensitivity analysis in identifying the key control parameters to improve the model-observation agreement. To apply the 4D-Var technique using CTMs, it is helpful to include additional information into the minimization procedure. The upper bounds of mixing ratios provided to the L-BFGS-B algorithm lead to a speed-up of the 4D-Var optimization.

The error statistics of the initial field used in our STEM-2K1 is lacking and was highly simplified in our analysis. The knowledge of such information is crucial to provide the optimal analysis in the future studies. Other than the initial field, the emission inventories and boundary conditions are far from accurate as well. In addition, the meteorological fields, physical parameters such as diffusion, and chemical reaction rates are also uncertain. Complete calibration of these uncertainties is a daunting task that can only be pursued

step by step. Nevertheless, a great promise of data assimilation is shown in its ability to blend the real measurements with our accumulated knowledge of atmospheric chemistry through CTMs.

In this paper we have demonstrated how the 4D-Var method can be used to assimilate aircraft data. The technique can be easily extended to assimilate observations from a variety of data sources (e.g., we are now assimilating ozone data from aircraft, surface networks, and ozonesondes). These results demonstrate that this analysis framework can integrate data from a variety of sources, and produce a 4-dimensional reanalysis field that represents a more realistic state of the atmosphere than provided by forward models alone. These results can be extended to provide a mission-wide reanalysis by extending the analysis for the entire period of the experiment. We believe that the value derived from large field experiments will be enhanced by such a closer integration of modeled and measured quantities. This improved estimate state better defines the spatial and temporal fields of key chemical components in relation to their sources and sinks. This information is critical in the interpretation of observational data such as those obtained during intensive field campaigns, and to more completely utilize the increasing amount of operational atmospheric chemical and aerosol data provided by satellite and monitoring networks. In addition this information can be used to help identify model deficiencies, and thus lead to better models, and ultimately an improvement in our capability to predict air-quality. Further efforts focused on improving the forward model are planned and needed.

Finally, results from such reanalysis studies should also provide important insights into experimental design. The 4D-Var framework allows us to assess the impact on the assim-

ilation results of adding additional observations of different species, and different combinations, as well as exploring issues related to time resolution (e.g., using 10-second versus 3-minute average values in the assimilation), and spatial sampling.

Acknowledgments. The authors gratefully thank the National Science Foundation for the support through the award NSF ITR AP&IM 0205198. This work was also supported by NASA GTE TRACE-P, ACMAP, and the NSF Atmospheric Chemistry program. The work of A. Sandu was partially supported by the award NSF CAREER ACI 0093139.

References

Benjamin, S. G., et al. (2004), An hourly assimilation-forecast cycle: The RUC, *Monthly Weather Review*, *132*(2), 495–518.

Byrd, R., P. Lu, and J. Nocedal (1995), A limited memory algorithm for bound constrained optimization, *SIAM J. Sci. Stat. Comput.*, *16*(5), 1190–1208.

Carmichael, G. R., D. N. Daescu, A. Sandu, and T. Chai (2003a), Computational aspects of chemical data assimilation into atmospheric models, in *Computational Science - ICCS 2003*, no. IV in Lecture Notes in Computer Science, pp. 269–278, Springer-Verlag Berlin.

Carmichael, G. R., et al. (2003b), Regional-scale chemical transport modeling in support of the analysis of observations obtained during the TRACE-P experiment, *J. of Geophys. Res.*, *108*(D21), Art. No. 8823.

Carter, W. (2000), Documentation of the SAPRC-99 chemical mechanism for VOC reactivity assessment, *Tech. Rep. 92-329*, California Air Resources Board Contract.

Clerbaux, C., J. Hadji-Lazaro, D. Hauglustaine, G. Megie, B. Khattatov, and J. F. Lamarque (2001), Assimilation of carbon monoxide measured from satellite in a three-

dimensional chemistry-transport model, *J. of Geophys. Res.*, *106*(D14), 15,385–15,394.

Daescu, D. N., and G. R. Carmichael (2003), An adjoint sensitivity method for the adaptive location of the observations in air quality modeling, *J. Atmos. Sci.*, *60*, 434–449.

Daescu, D. N., G. R. Carmichael, and A. Sandu (2000), Adjoint implementation of rosenbrock methods applied to variational data assimilation problems, *J. Comput. Physics*, *165*(2), 496–510.

Daescu, D. N., A. Sandu, and G. R. Carmichael (2003), Direct and adjoint sensitivity analysis of chemical kinetic systems with KPP: II – numerical validation and applications, *Atmos. Environ.*, *37*, 5097–5114.

Elbern, H., and H. Schmidt (1999), A 4D-Var chemistry data assimilation scheme for Eulerian chemistry transport modeling, *J. of Geophys. Res.*, *104*(D15), 18,583–18,598.

Elbern, H., and H. Schmidt (2001), Ozone episode analysis by four-dimensional variational chemistry data assimilation, *J. of Geophys. Res.*, *106*(D4), 3569–3590.

Elbern, H., H. Schmidt, and A. Ebel (1997), Variational data assimilation for tropospheric chemistry modeling, *J. of Geophys. Res.*, *102*(D13), 15,967–15,985.

Elbern, H., H. Schmidt, O. Talagrand, and A. Ebel (2000), 4D-variational data assimilation with an adjoint air quality model for emission analysis, *Environmental Modeling and Software*, *15*, 539–548.

Errera, Q., and D. Fonteyn (2001), Four-dimensional variational chemical assimilation of CRISTA stratospheric measurements, *J. of Geophys. Res.*, *106*(D11), 12,253–12,265.

Fisher, M., and D. J. Lary (1995), Lagrangian four-dimensional variational data assimilation of chemical species, *Quart. J. Roy. Meteor. Soc.*, *121*, 1681–1704.

Hanea, R. G., G. J. M. Velders, and A. Heemink (2004), Data assimilation of ground-level ozone in Europe with a kalman filter and chemistry transport model, *J. of Geophys. Res.*, *109*(D10), Art. No. D10,302.

Hoelzemann, J. J., H. Elbern, and A. Ebel (2001), SAS and 4D-var data assimilation for chemical state analysis by urban and rural observation sites, *Physics and chemistry of the earth part B-Hydrology oceans and atmosphere*, *26*(10), 807–812.

Houtekamer, P. L., L. M. Herschel, G. Pellerin, M. Buehner, M. Charron, L. Spacek, and B. Hansen (2005), Atmospheric data assimilation with an ensemble Kalman filter: Results with real observations, *Monthly Weather Review*, in press.

Klinker, E., F. Rabier, G. Kelly, and J. F. Mahfouf (2000), The ECMWF operational implementation of four-dimensional variational assimilation. III: Experimental results and diagnostics with operational configuration, *Quart. J. Roy. Meteor. Soc.*, *126*(564), 1191–1215.

Lamarque, J. F., and J. C. Gille (2003), Improving the modeling of error variance evolution in the assimilation of chemical species: Application to MOPITT data, *Geophysical Research Letters*, *30*(9), Art. No. 1470.

Lamarque, J. F., B. V. Khattatov, and J. C. Gille (2002), Constraining tropospheric ozone column through data assimilation, *J. of Geophys. Res.*, *107*(D22), Art. No. 4651.

Lamarque, J. F., et al. (2004), Application of a bias estimator for the improved assimilation of Measurements of Pollution in the Troposphere (MOPITT) carbon monoxide retrievals, *J. of Geophys. Res.*, *109*(D16), Art. No. D16,304.

Mahfouf, J. F., and F. Rabier (2000), The ECMWF operational implementation of four-dimensional variational assimilation. II: Experimental results with improved physics,

Quart. J. Roy. Meteor. Soc., *126*(564), 1171–1190.

Menut, L. (2003), Adjoint modelling for atmospheric pollution processes sensitivity at regional scale during the ESQUIF IOP2, *J. of Geophys. Res.*, *108*(D17), Art. No. 8562.

Menut, L., R. Vautard, M. Beekmann, and C. Honor (2000), Sensitivity of photochemical pollution using the adjoint of a simplified chemistry-transport model, *J. of Geophys. Res.*, *105-D12*(15), 15,379–15,402.

Miehe, P., A. Sandu, G. R. Carmichael, Y. Tang, and D. Daescu (2002), A commmunication library for the parallelization of air quality models on structured grids, *Atmos. Environ.*, *36*, 3917–3930.

Pielke, R. A., et al. (1992), A comprehensive meteorological modeling system - RAMS, *Meteorol. Atmos. Phys.*, *49*, 69–91.

Rabier, F., H. Jarvinen, E. Klinker, J. F. Mahfouf, and A. Simmons (2000), The ECMWF operational implementation of four-dimensional variational assimilation. I: Experimental results with simplified physics, *Quart. J. Roy. Meteor. Soc.*, *126*(564), 1143–1170.

Sandu, A., D. N. Daescu, and G. R. Carmichael (2003), Direct and adjoint sensitivity analysis of chemical kinetic systems with KPP: I – theory and software tools, *Atmos. Environ.*, *37*, 5083–5096.

Sandu, A., D. Daescu, G. R. Carmichael, and T. Chai (2005), Adjoint sensitivity analysis of regional air quality models, *J. Comput. Physics*, in press.

Schmidt, H., and D. Martin (2003), Adjoint sensitivity of episodic ozone in the Paris area to emissions on the continental scale, *J. of Geophys. Res.*, *108*(D17), Art. No. 8561.

Segers, A. J., A. W. Heemink, M. Verlaan, and M. van Loon (2000), A modified RRSQRT-filter for assimilating data in atmospheric chemistry models, *Environmental Modeling*

and Software, *15*, 663–671.

Streets, D. G., K. F. Yarber, J.-H. Woo, and G. R. Carmichael (2003), Biomass burning in asia: annual and seasonal estimates and atmospheric emissions, *J. of Geophys. Res.*, *108*(D21), Art. No. 8809.

van Loon, M., P. J. H. Builtjes, and A. J. Segers (2000), Data assimilation of ozone in the atmospheric transport and chemistry model LOTOS, *Environmental Modeling and Software*, *15*, 603–609.

Woo, J.-H., et al. (2003), Contribution of biomass and biofuel emissions to trace gas distributions in Asia during the TRACE-P experiment, *J. of Geophys. Res.*, *108*(D21), Art. No. 8812.

Zhang, X. F., A. W. Heemink, L. H. J. M. Janssen, P. H. M. Janssen, and F. J. Sauter (1999), A computationally efficient Kalman smoother for the evaluation of the ch_4 budget in europe, *Appl. Math. Modelling*, *23*(2), 109–129.

Zhu, C., R. H. Byrd, and J. Nocedal (1997), L-BFGS-B–fortran routines for large scale bound constrained optimization, *ACM Trans. Math. Software*, *23*(4), 550–560.

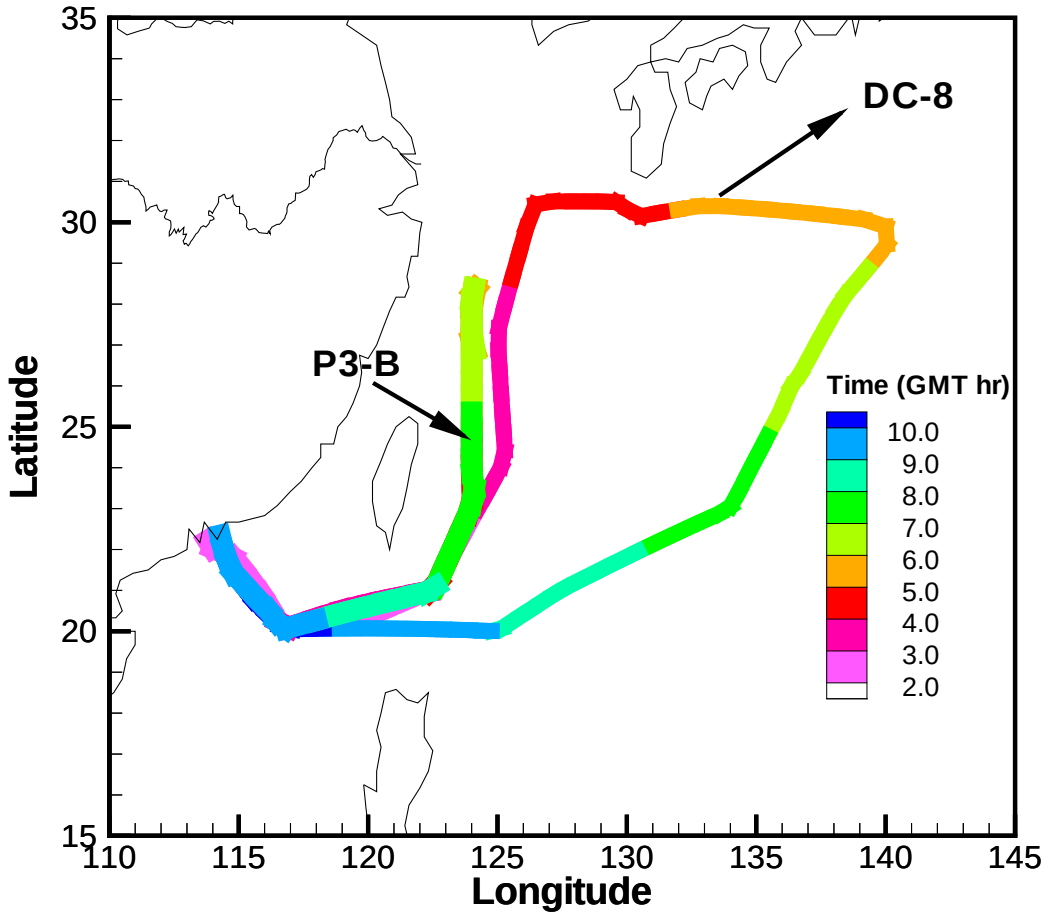

Figure 1. Flight routes of the DC-8 and the P3-B on March 7, 2001. The P3-B return trajectory overlaps with and hides the first part of the trajectory.

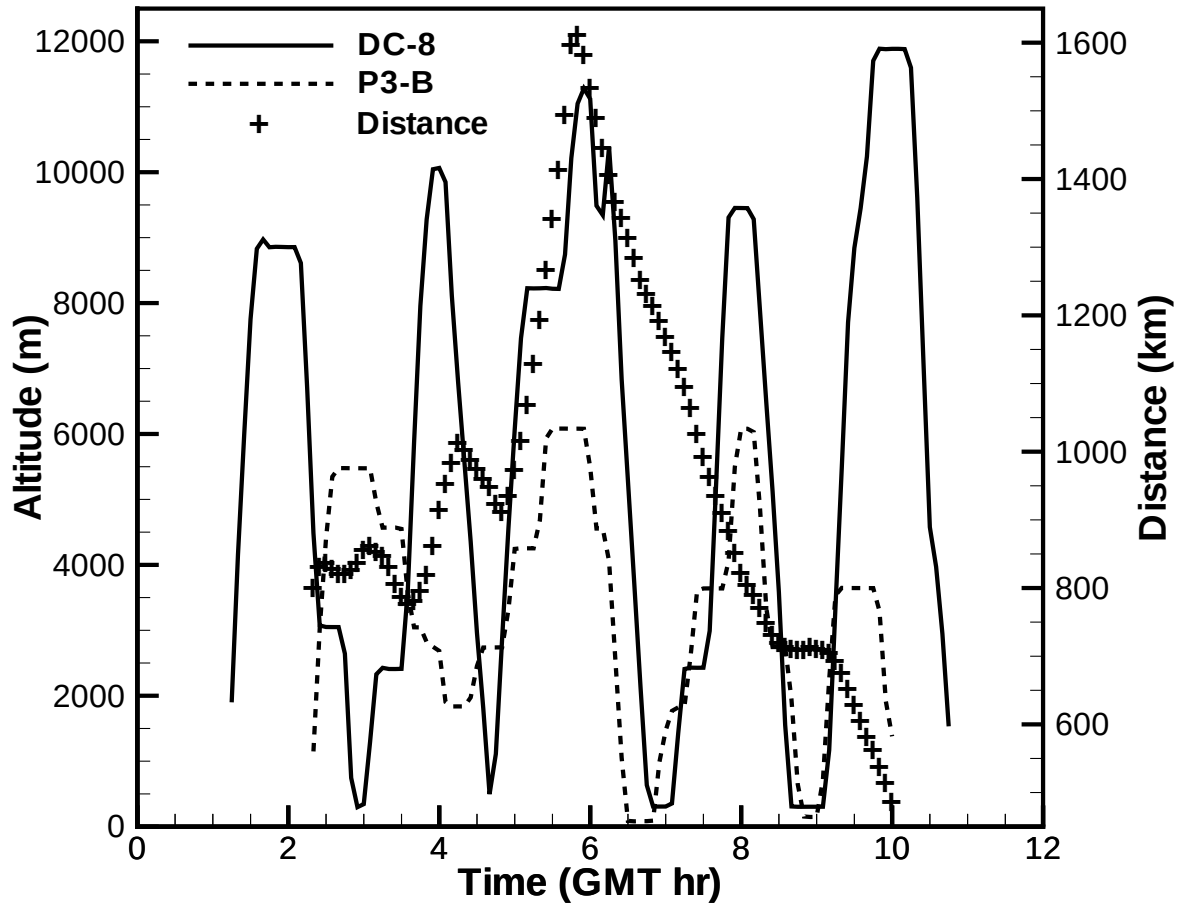

Figure 2. Time series of flight heights of the DC-8 and the P3-B on March 7, 2001. The distances between the two aircrafts are also shown.

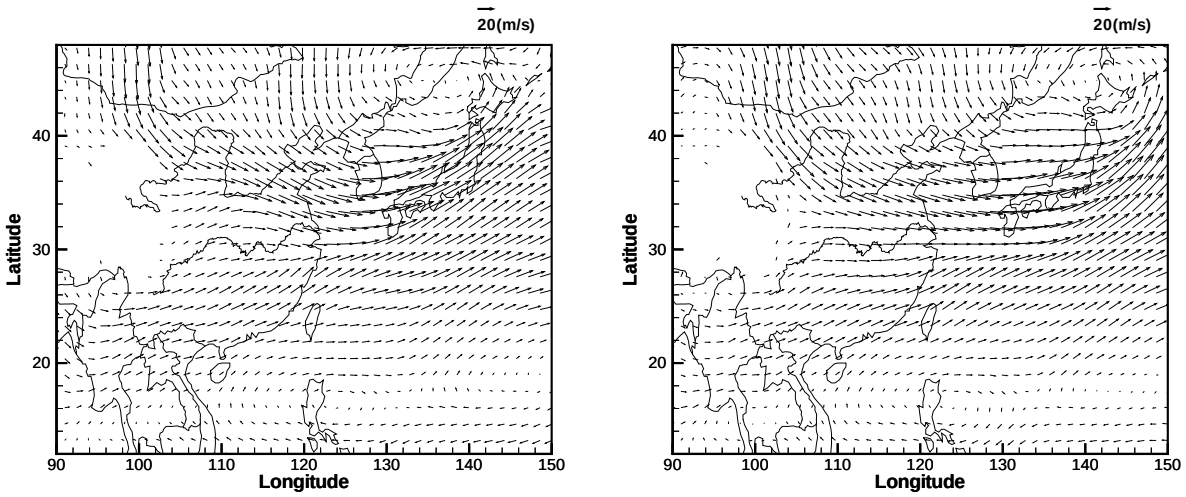

Figure 3. Wind fields at z=3.5 km. Left: 0 GMT; Right: 9 GMT.

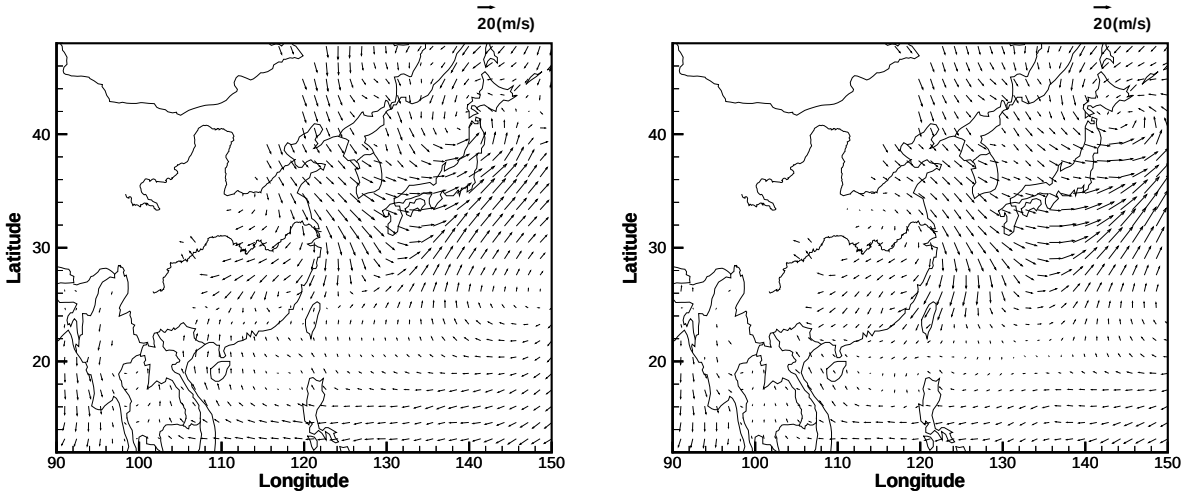

Figure 4. Wind fields at z=1.0 km. Left: 0 GMT; Right: 9 GMT.

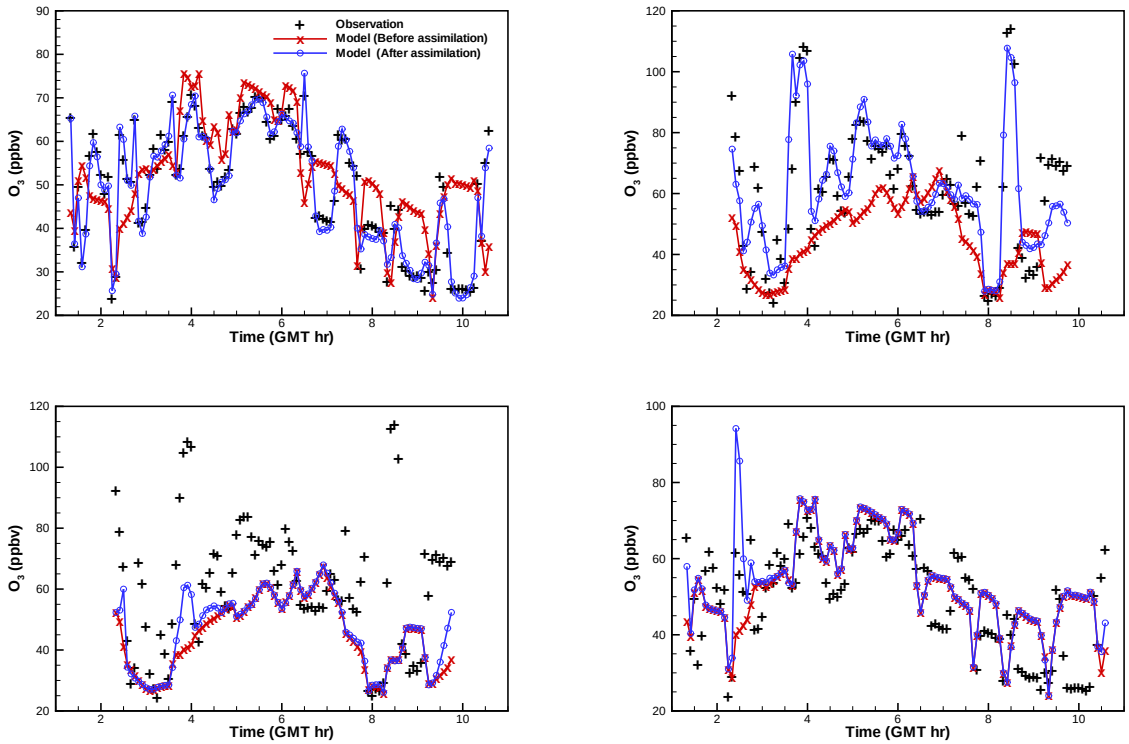

Figure 5. Results of the O_3 assimilation tests. The flight measurements and their corresponding model predictions are shown. Left: Results of the test that assimilated the DC-8 O_3 observations. Right: Results of the test that assimilated the P3-B O_3 observation. Top: Assimilated flight observations. Bottom: Held observations from the other flight.

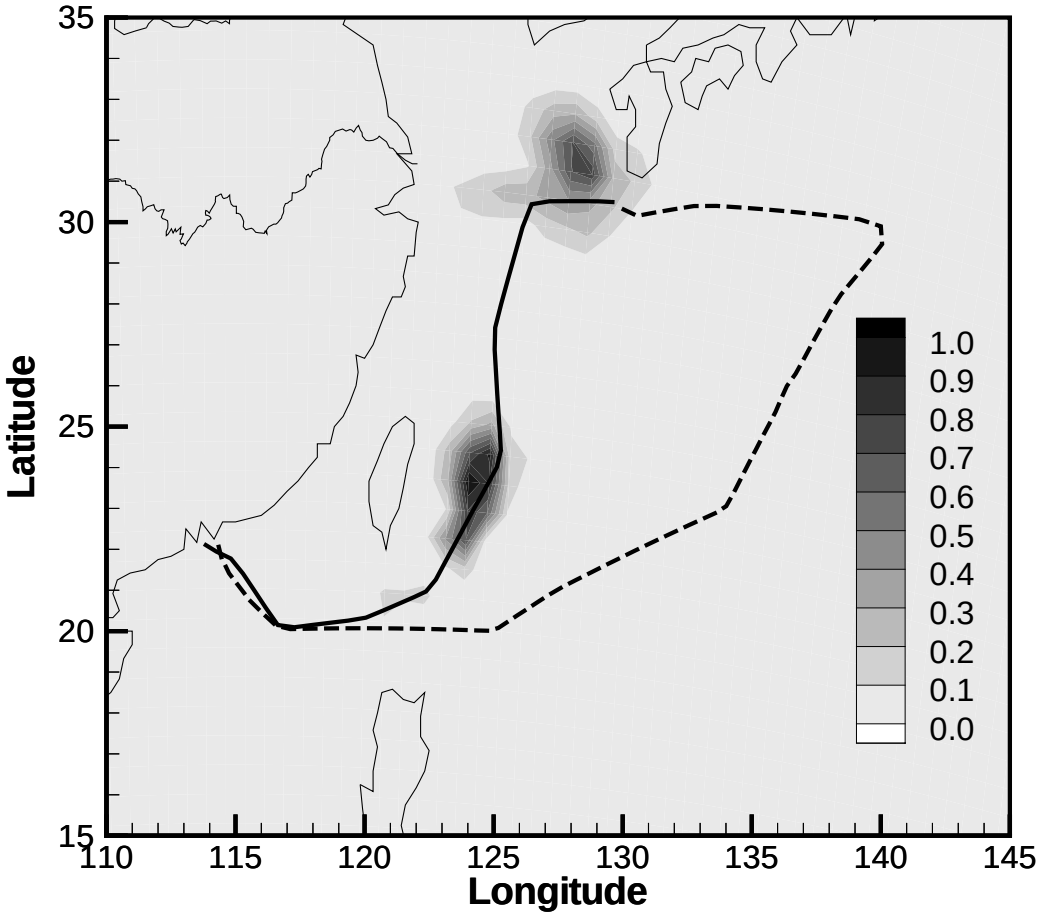

Figure 6. A top view of the "cones of influence" by ozone. The maximum $\mathcal{C}(x)$ over 18 vertical levels is chosen at each geographical location. The values shown are normalized. The flight track of the DC-8 is also shown, where the dashed line is after 4:40 GMT.

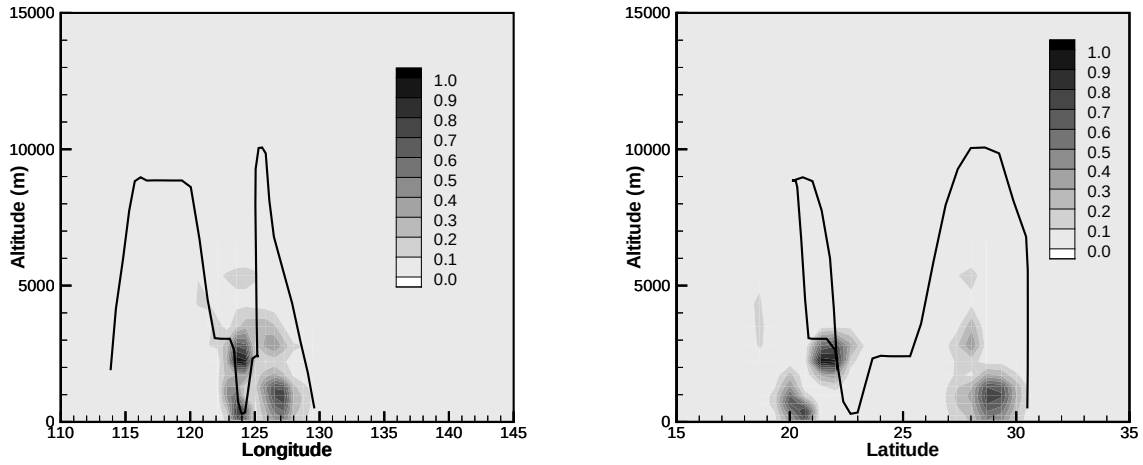

Figure 7. A south view (left) and an east view (right) of the "cones of influence" by ozone. The projection is made by choosing the maximum value in the projection direction. The values shown are normalized. The flight track of the DC-8 before 4:40 GMT is also shown.

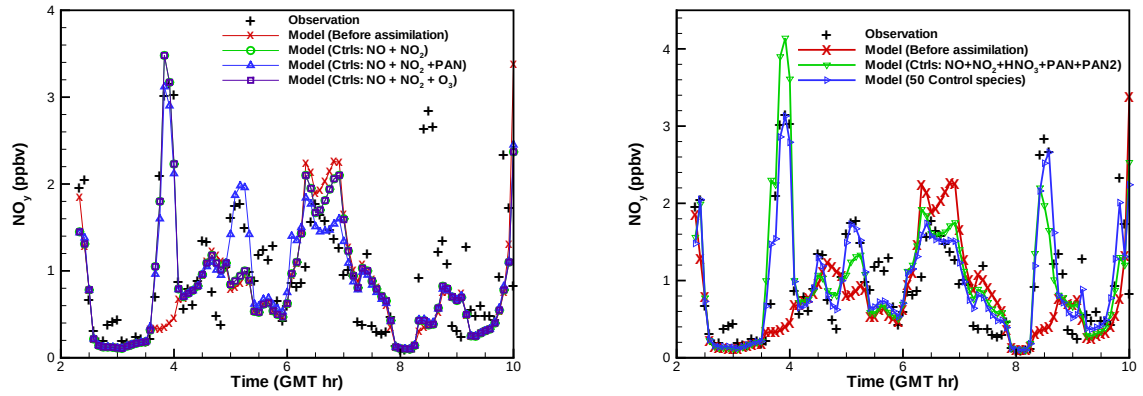

Figure 8. Data assimilation results of using different control variables in assimilating NO_y.

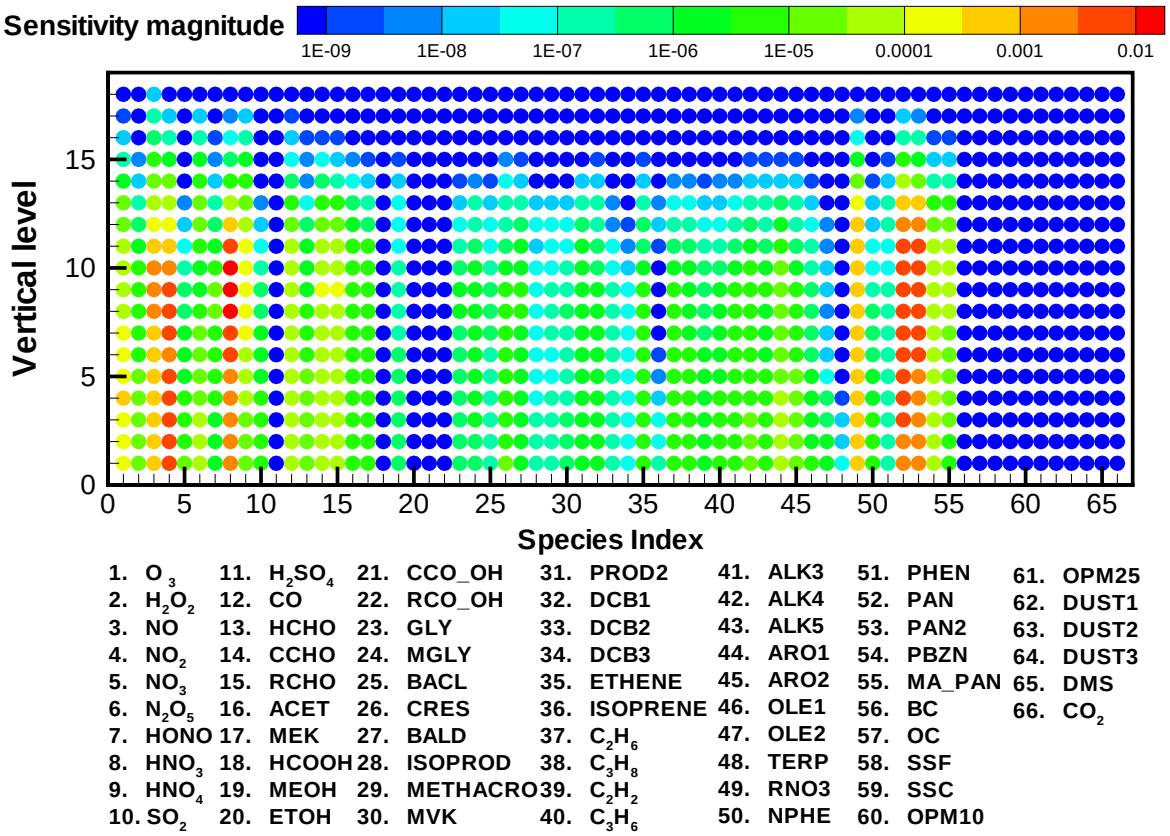

Figure 9. Sensitivity of NO_y predictions with respect to initial conditions at different levels for 66 prognostic species. Averaged magnitudes of gradients are shown. Species refer to the SAPRC-99 chemical mechanism, and full species represented can be found in Carter (2000).

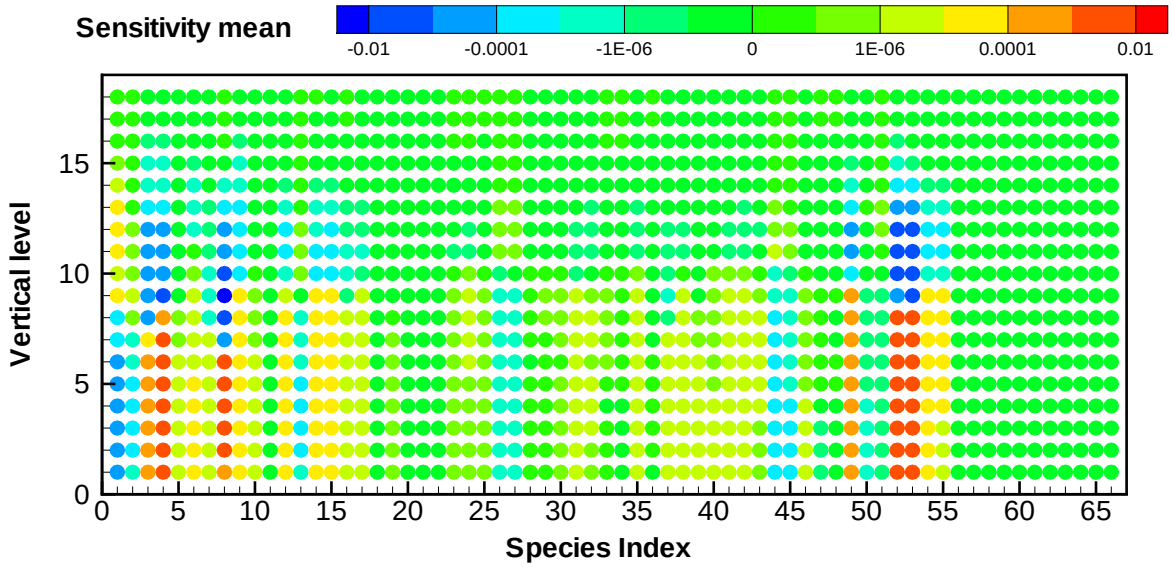

Figure 10. Sensitivity of NO_y predictions with respect to initial conditions at different levels for 66 prognostic species. Mean gradients are shown. See Figure 9 for names of the species.

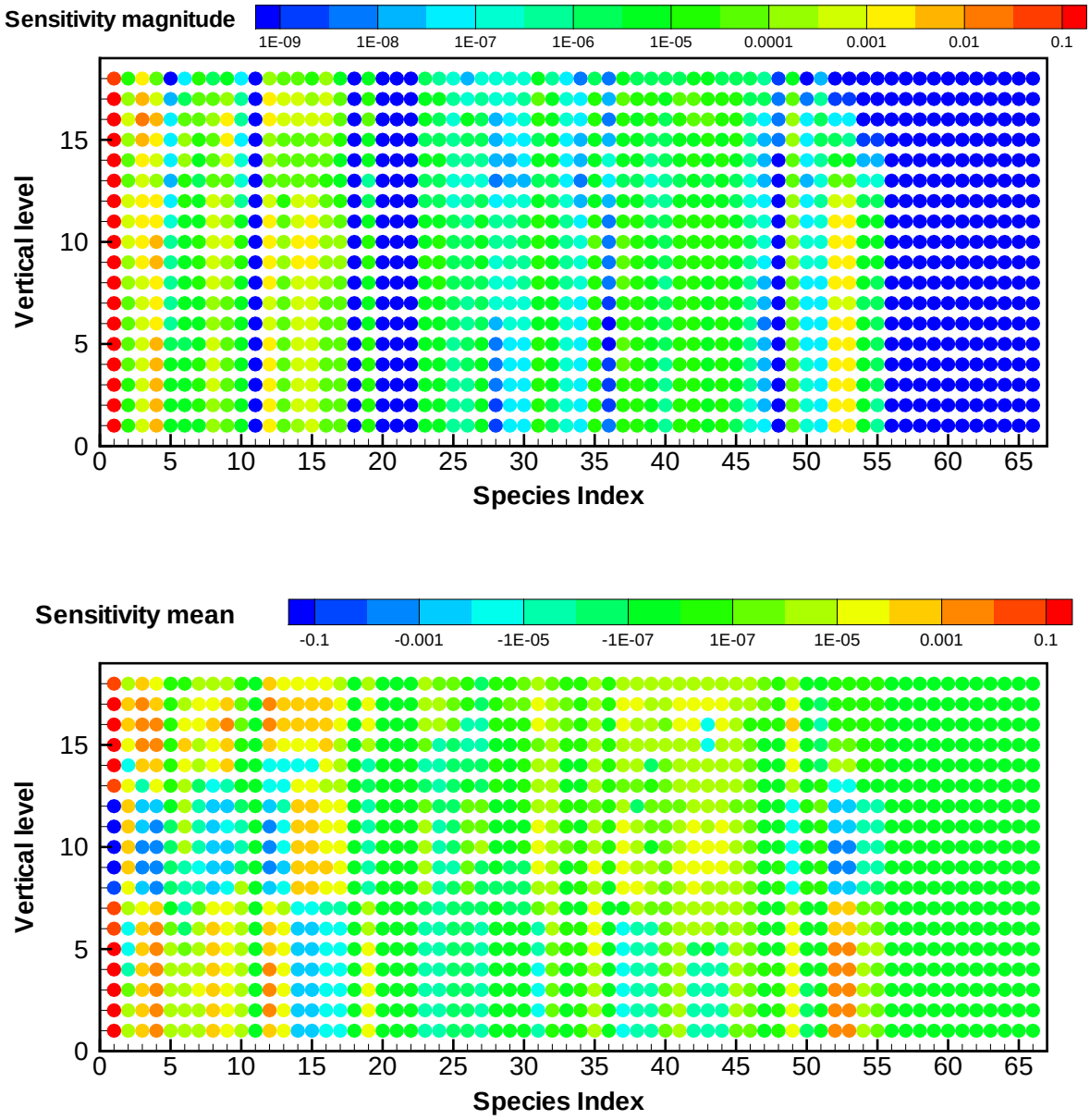

Figure 11. Sensitivity of O_3 predictions with respect to initial conditions at different levels for 66 prognostic species. Averaged magnitudes of gradients (top) and mean gradients (bottom) are shown. See Figure 9 for names of the species.

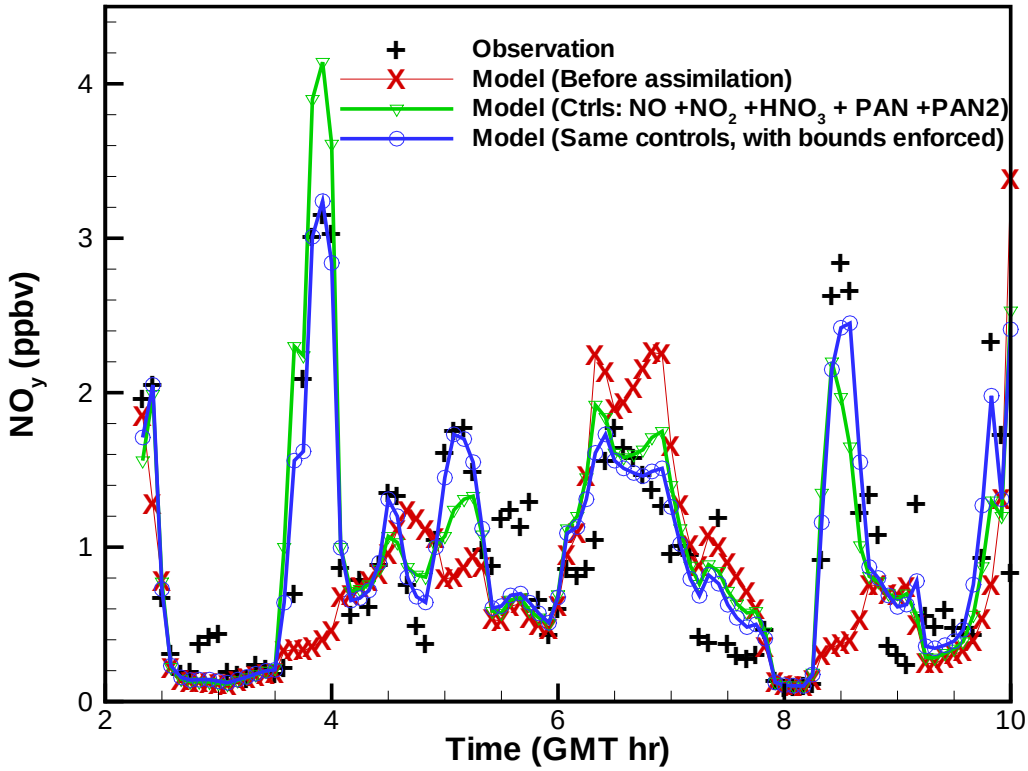

Figure 12. Data assimilation results show the effect of enforcing upper bounds through L-BFGS-B in 4D-Var.

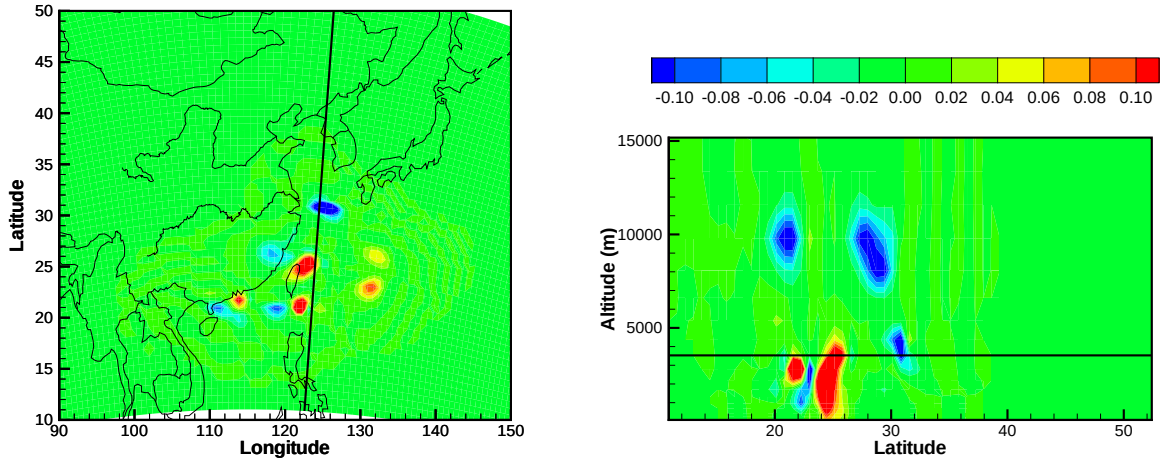

Figure 13. Relative changes in initial O_3 after assimilating the P3-B NO_y measurements. Left: at z=3.5 km; Right: vertical cross section, (position shown on the left).

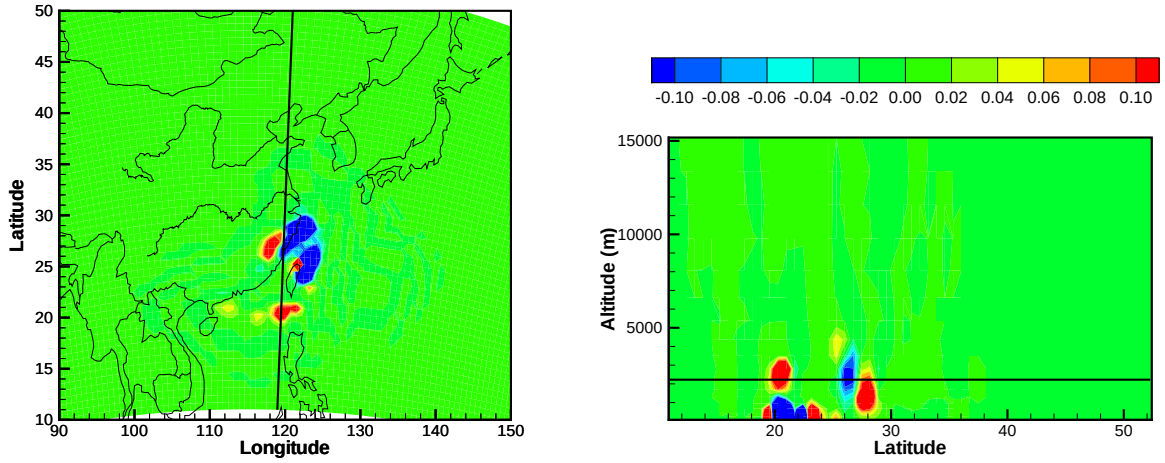

Figure 14. Relative changes in initial NO_2 after assimilating the P3-B NO_y measurements. Left: at z=2.2 km; Right: vertical cross section, (position shown on the left).

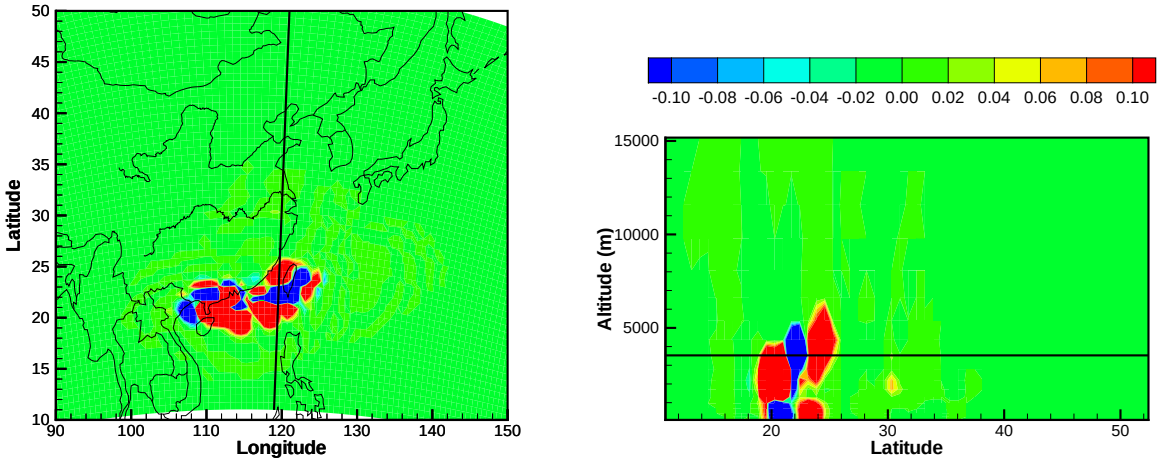

Figure 15. Relative changes in initial HNO_3 after assimilating the P3-B NO_y measurements. Left: at z=3.5 km; Right: vertical cross section, (position shown on the left).

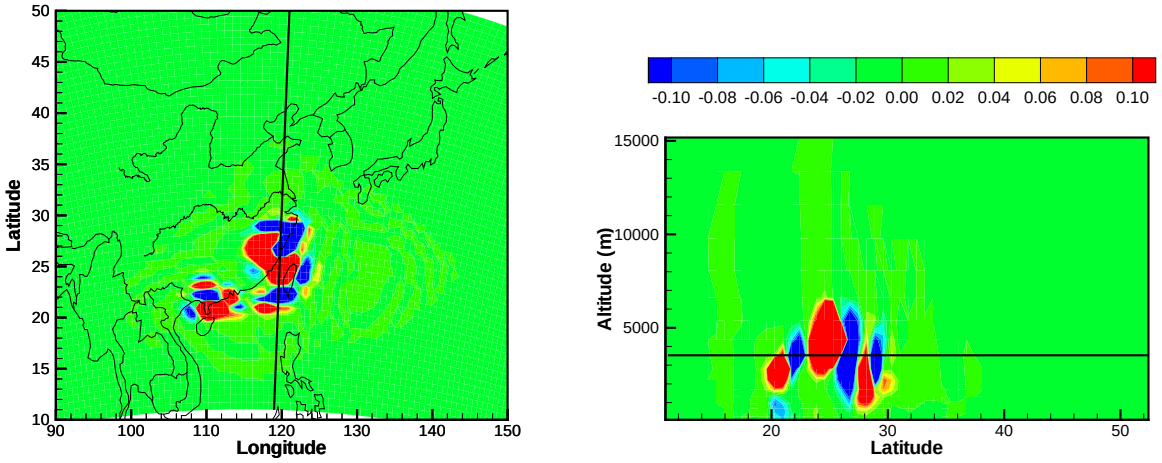

Figure 16. Relative changes in initial PAN after assimilating the P3-B NO_y measurements. Left: at z=3.5 km; Right: vertical cross section, (position shown on the left).

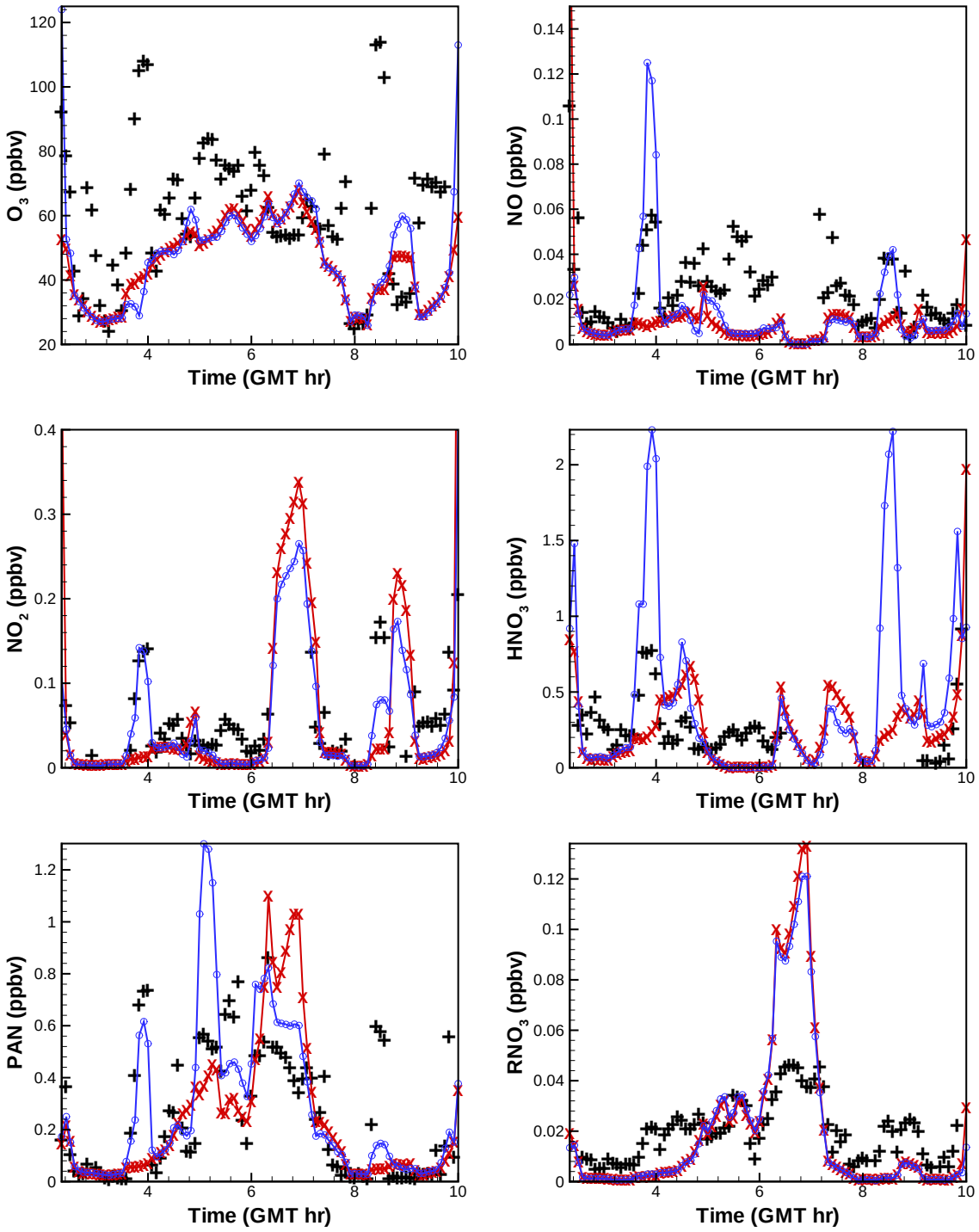

Figure 17. Model predictions before (shown in red) and after (shown in blue) assimilation of the P3-B NO_y measurements. The measurements of the 6 species, shown as "+", were not assimilated.

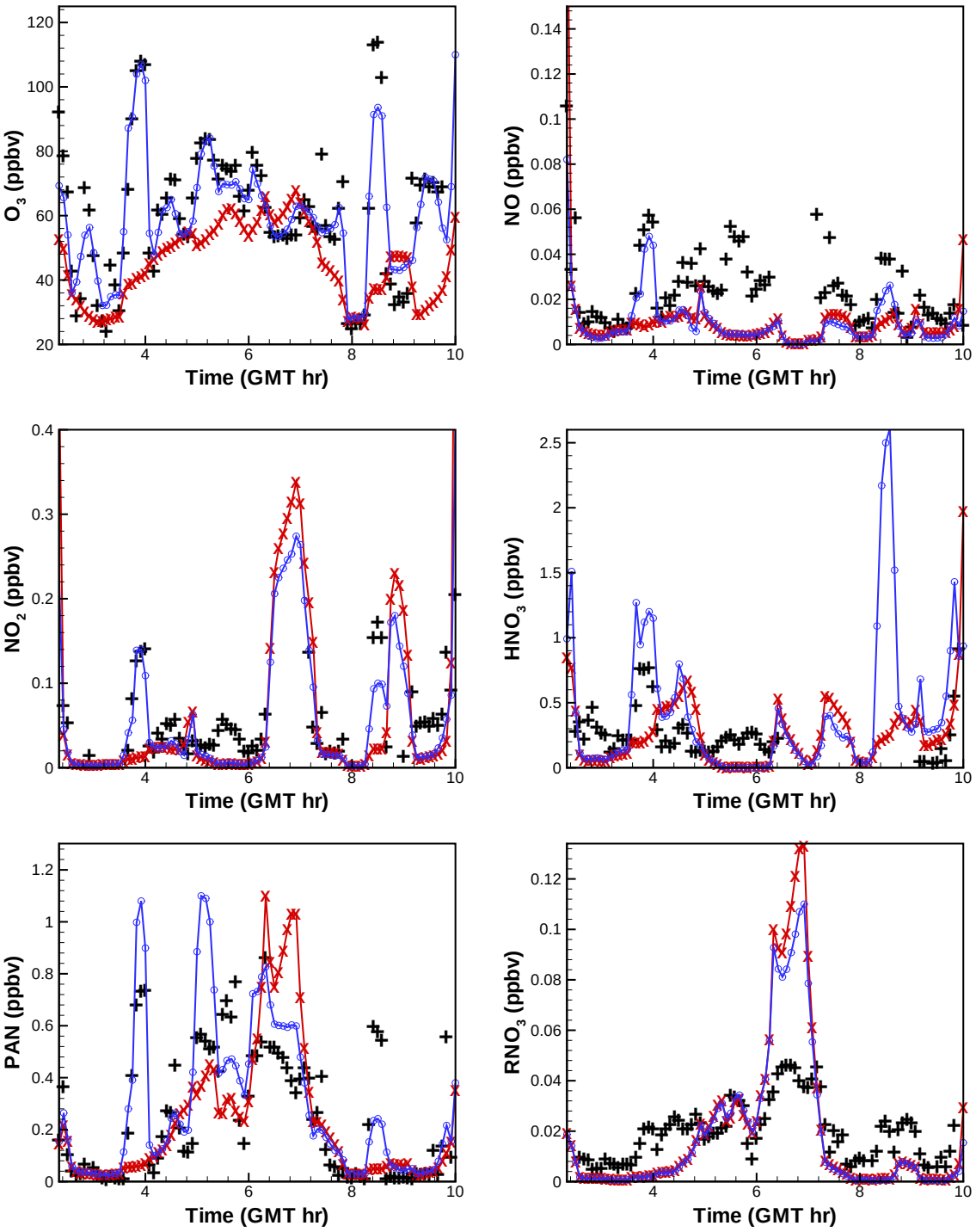

Figure 18. Model predictions before (red) and after (blue) assimilating the P3-B measurements ("+") of 6 species.

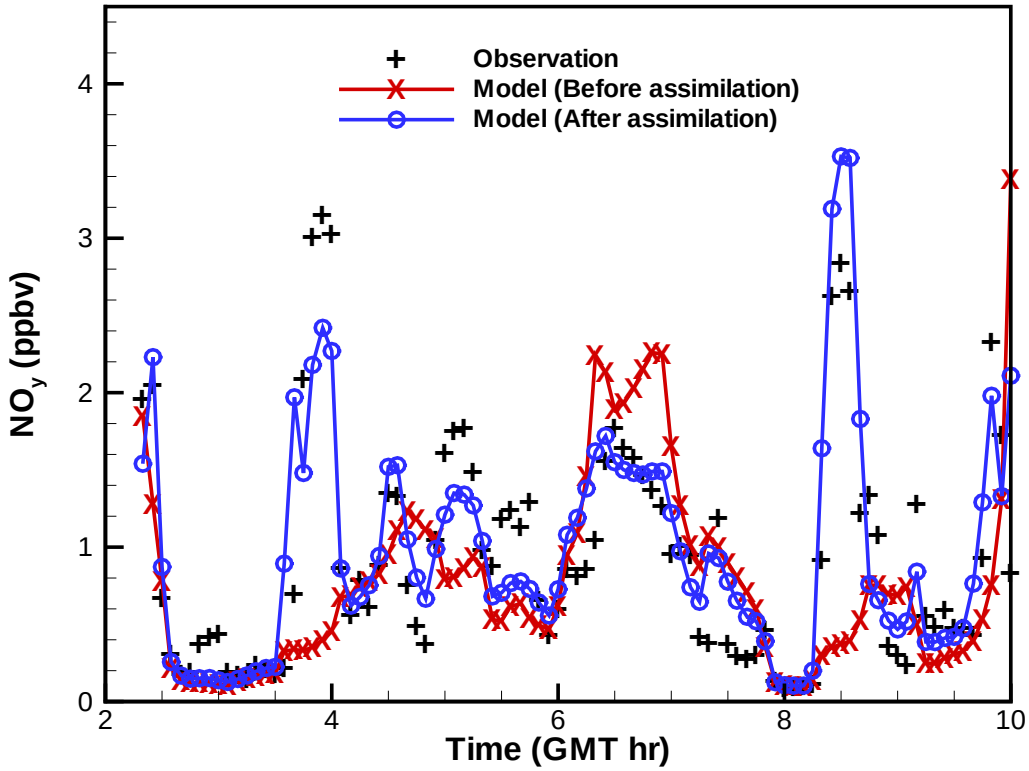

Figure 19. Model predictions of NO_y before and after assimilating O_3, NO, NO_2, HNO_3, PAN, and RNO_3 measurements. The NO_y measurements were not used in the assimilation test.

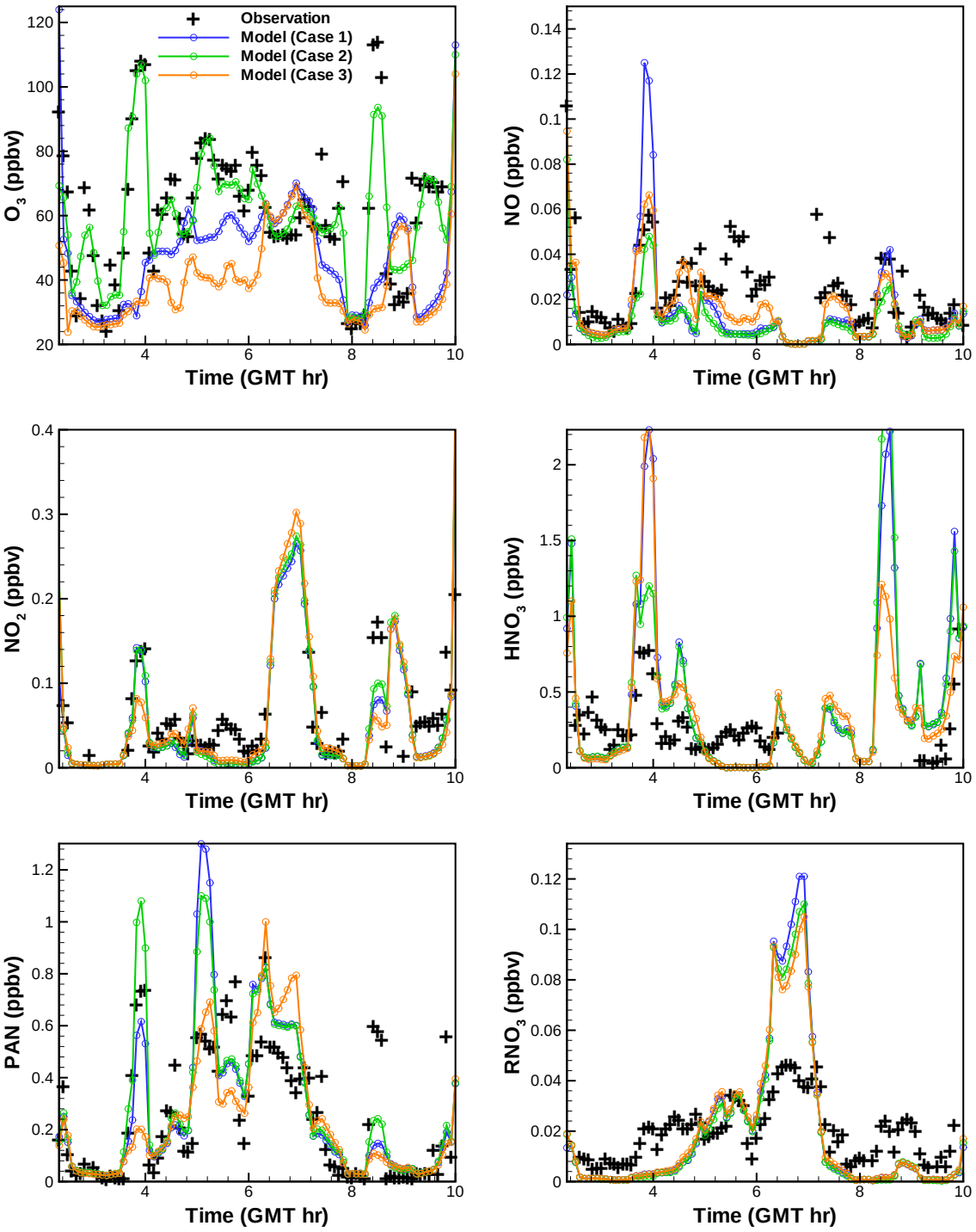

Figure 20. Comparison of model predictions between three assimilation tests. The measurements that were assimilated: Case 1, NO_y; Case 2, O_3, NO, NO_2, HNO_3, PAN, and RNO_3; Case 3, NO_y, NO, NO_2, HNO_3, PAN, and RNO_3. All measurements are from the P3-B.

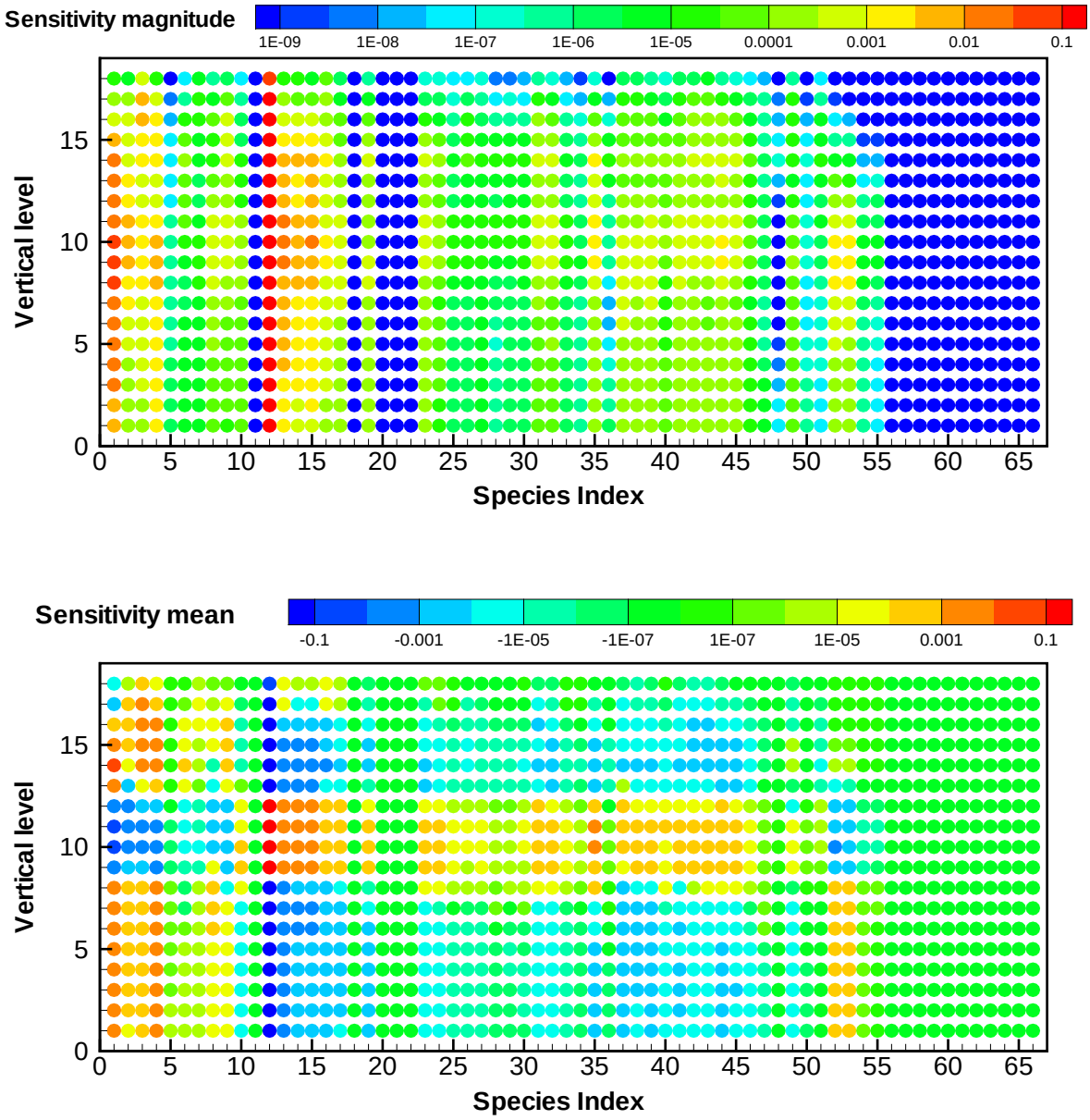

Figure 21. Sensitivity of *CO* predictions with respect to initial conditions at different levels for 66 prognostic species. Averaged magnitudes of gradients (top) and mean gradients (bottom) are shown. See Figure 9 for names of the species.

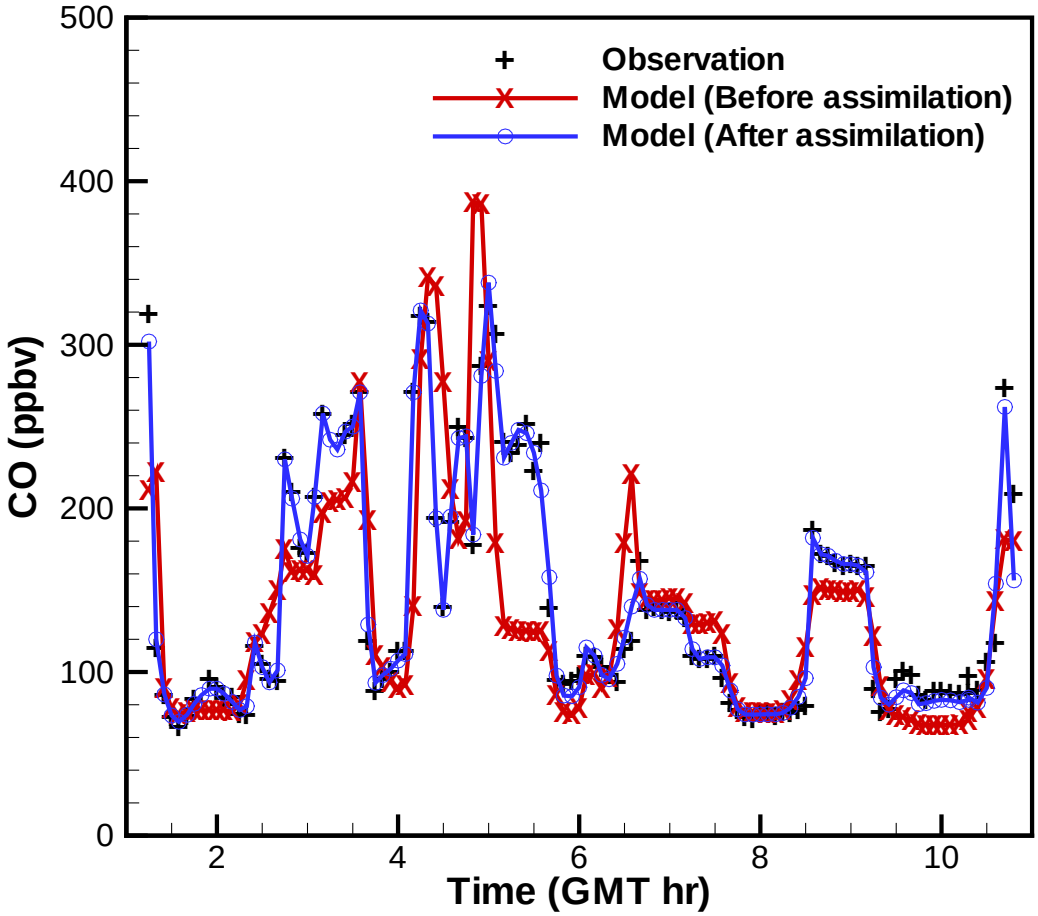

Figure 22. Results of a *CO* assimilation test. The DC-8 observations were assimilated.